Computers and Chemical Engineering 185 (2024) 108664

Contents lists available at ScienceDirect

Computers and Chemical Engineering

journal homepage: www.elsevier.com/locate/cace

Nonlinear observer for online concentration estimation in vanadium flow batteries based on half-cell voltage measurements

Thomas Puleston [a,*], Andreu Cecilia [b], Ramon Costa-Castelló [a,b], Maria Serra [a,b]

[a] Institut de Robòtica i Informàtica Industrial, CSIC-UPC, C/ Llorens i Artigas 4-6, 08028, Barcelona, Spain
[b] Universitat Politècnica de Catalunya, Diagonal 647, 08028, Barcelona, Spain

ARTICLE INFO

Keywords:
Vanadium flow batteries
Nonlinear observer
State of Charge
Battery monitoring
Electrolyte imbalance

ABSTRACT

This paper presents a nonlinear observer to estimate the active species concentrations in vanadium flow batteries. To conduct the estimation, the observer relies only on current, flow rate and two half-cell voltage measurements. In contrast to previous works in the field, the proposed observer is capable to deal simultaneously with two significant and challenging conditions: (1) a not necessarily high flow rate, which results in different concentrations for tanks and cells, and (2) presence of crossover and oxidation side reactions, that result in imbalance between the electrolytes on the positive and negative sides of the system. The stability and convergence of the observer are formally demonstrated using a Lyapunov analysis and subsequently validated through comprehensive computer simulations. Finally, utilising the information provided by the observer, a strategy to independently regulate the flow rate of each electrolyte based on their individual state of charge is developed.

1. Introduction

Redox Flow Batteries (RFB) are emerging as one of the most promising energy storage systems for large-scale stationary applications (Kebede et al., 2022). Unlike conventional battery technologies, in RFB the fluid reactants are stored in tanks separated from the electrochemical reactor, resulting in a decoupling of energy and power (Guarnieri et al., 2018). The high degree of versatility and scalability associated to their unique architecture is combined with a respectable efficiency (75%–85%), low maintenance requirements and a minimal self discharge rate when inactive. In particular, the All-Vanadium Flow Battery (VFB) is the most mature flow battery technology, with important industrial-scale facilities in service worldwide (Zhang et al., 2021). By utilising vanadium as the only active element, they do not suffer from the cross-contamination problems that affect other types of RFB, resulting in a potentially very long cycle life (≈ 16000 cycles). In addition, they do not pose significant safety concerns because of the utilisation of an aqueous solution at room temperature and atmospheric pressure.

In spite of VFB remarkable advantages, their particular structure is also accompanied with some important challenges. One of them is their susceptibility to various undesired phenomena, such as vanadium crossover, as well as gassing and oxidation side reactions, that produce a discrepancy of active species concentrations in both sides of the system (Huang and Mu, 2021; Nolte et al., 2021). This condition, known as electrolyte imbalance, results in capacity loss and, when unnoticed, can lead to even more severe consequences such as electrodes corrosion or membrane damage (Puleston et al., 2022; Jirabovornwisut and Arpornwichanop, 2019). On the other hand, another major challenge is the lack of a systematic method to measure online the concentrations of vanadium active species (Clemente and Costa-Castelló, 2020; Wang et al., 2023). The knowledge of these concentrations is crucial for the optimal operation of VFB systems, enabling:

1. To determine the system State of Charge (SoC) and State of Health (SoH) (Nolte et al., 2021; Puleston et al., 2024; Clemente et al., 2023). In turn, these indexes are essential for the integration of the battery into energy management systems, and planning its operation (Choi et al., 2016; Schubert et al., 2023).
2. To promptly detect faults and deviations in the system behaviour, and identify its possible causes. For instance, a fast crossover of vanadium towards one side of the system could be associated to a degraded membrane (Puleston et al., 2023; Tempelman et al., 2020). In contrast, a rapid change in the average oxidation state of the electrolytes could be an indicator of an incorrect sealing of the negative tank, or electrode degradation that leads to gassing side reactions (Nourani et al., 2019).

* Corresponding author.
E-mail address: tpuleston@iri.upc.edu (T. Puleston).

https://doi.org/10.1016/j.compchemeng.2024.108664
Received 29 December 2023; Received in revised form 11 March 2024; Accepted 13 March 2024
Available online 15 March 2024
0098-1354/© 2024 The Author(s). Published by Elsevier Ltd. This is an open access article under the CC BY license (http://creativecommons.org/licenses/by/4.0/).

3. To identify the optimal strategy to recover imbalanced electrolytes, as well as to conduct these strategies effectively (Poli et al., 2021; Pichugov et al., 2023; Puleston et al., 2024).
4. To implement enhanced control strategies oriented to maximise the energy efficiency (e.g., flow rate regulation (König et al., 2016; Jirabovornwisut et al., 2020; Guarnieri et al., 2020)), and minimise the degradation of the VFB components (e.g., avoiding overcharging and side reactions (Wang et al., 2023; Akter et al., 2019)).
5. To estimate the parameters that govern the kinetics of the electrochemical reactions (Choi et al., 2016; He et al., 2022). In turn, these are needed to calculate the electrodes overpotential and the relative contribution of the different losses, providing valuable insights for optimising battery performance.

Several experimental methods have been explored in the literature to determine the composition of the electrolytes. The simplest one is to include an auxiliary open circuit voltage cell, and compute the concentrations by solving the Nernst equation (Bogdanov et al., 2023). However, that approach proves effective only when the electrolytes in both sides of the system are perfectly balanced and the total vanadium concentration is known in advance (Nolte et al., 2021). In laboratory-scale setups, potentiometric titration is a viable candidate to determine the exact concentration of each species in an electrolyte sample (Geiser et al., 2019). However, it is time consuming and results impractical for online monitoring in industrial-scale applications. Spectroscopic methods, such as UV/Vis, appear also as an appealing option, given the difference in colour presented by each type of vanadium ion. Nonetheless, to obtain an accurate measurement, costly equipment is required and, furthermore, they can only work in a limited range of electrolyte concentrations (Loktionov et al., 2022; Rybalchenko et al., 2022). Several groups are currently working on the development of alternative experimental methods, such as those based on ultrasonic measurements (Yan et al., 2023; Zang et al., 2019), novel micro-electrodes for amperometric analysis (Neyhouse et al., 2021; Zub et al., 2022) or coulometric sensors that make use of auxiliary cells (Loktionov et al., 2023).

To eliminate the need of costly and complex sensing equipment, the development of model-based algorithms that estimate the variables of interest only from easily measurable signals is gaining increasing attention (Puleston et al., 2022; Clemente and Costa-Castelló, 2020). Most of the estimation works available in VFB literature rely on Equivalent Circuit Models (ECM), that utilise electric elements to characterise the electrical dynamic behaviour of the battery (Zhang et al., 2015; Xiong et al., 2019). Some authors (Wei et al., 2016; Zhao et al., 2022; Khaki and Das, 2021) resorted to algorithms based on Extended Kalman Filters (EKF) to estimate the electric parameters of an ECM together with the battery's SoC, only from current and voltage measurements. To consider possible degradation in the battery condition, an empirical capacity loss factor was introduced and combined with a Sliding Mode Observer (SMO) (Xiong et al., 2017) and an EKF (Wei et al., 2018) to conduct a co-estimation of capacity and SoC. Finally, Fornaro et al. (2022, 2023) developed a methodology based on the combination of sliding mode differentiators and a recursive least squares algorithm to estimate the model parameters, the SoC, and the SoH in the context of wind-power based applications. The main limitation of the ECM approach is that most of their parameters lack of a clear physical interpretation and, furthermore, they do not take into account some of the key phenomena that influence VFBs behaviour, such as varying flow rates or electrolyte imbalance. Hence, they do not allow to obtain the individual electrolyte concentrations nor do they consider the effects of the various side reactions that typically affect VFB systems.

Another viable estimation approach involves the use of computational-efficient electrochemical models, where dynamic equations are grounded in conservation balances, providing each term with a precise physical meaning. This approach was followed by some authors Clemente et al. (2021, 2023), who utilised a SMO and a nonlinear observer to estimate the battery's SoC from current, flow rate and voltage measurements. Although they succeed in capturing the effects of the electrolyte flow rates, they still preserve some classic hypothesis regarding the electrolyte imbalance: side reactions that produce oxidation/reduction of the electrolyte are neglected, and the mass in both sides of the system is assumed to be constant and known. Indeed, Jienkulsawad et al. (2020) showed that, from the estimation point of view, it is impossible to reconstruct the complete concentration map utilising a single voltage measurement. This problem is partially solved through a model-based observer capable to deal with the different types of electrolyte imbalance that affect VFB systems (Puleston et al., 2023). However, the proposal requires of some prior knowledge regarding the overall average oxidation state of the system and, furthermore, it is imposed a "high flow rate" hypothesis that equalises tanks and cells concentrations, while presenting high sensitivity to sensor noise.

To overcome the existing limitations regarding concentration estimation, this paper presents a novel nonlinear observer that utilises half-cell voltage measurements against reference electrodes to estimate in real-time the concentrations of the four vanadium species present in a VFB system. The proposal does not require prior knowledge regarding the electrolyte imbalance status, and can be applied to systems where the high flow rate hypothesis is not satisfied, hence being able to distinguish between tanks and cells concentrations. Additionally, the observer presents a minimal set of parameters which can be easily tuned to obtain a good trade-off between convergence rate and noise sensitivity. Moreover, the observer includes an additional feedback term that constraints the estimates to realistic values, even in the convergence period. To the best of the authors knowledge, this is the first observer in the context of VFB that satisfies these characteristics. Finally, relying on the remarkable performance of the proposed observer, this paper proposes a regulation strategy of the flow rate of each electrolyte based on the estimation of the individual state of charge.

2. Dynamic model

This section introduces the model that describes the VFB dynamics, including realistic assumptions made to obtain a simplified representation that will be used in the remainder of this work.

2.1. System description

In a VFB two reservoirs store solutions containing vanadium active species dissolved in sulfuric acid, namely, the electrolytes. The negative side's electrolyte contains V^{2+} and V^{3+}, while the positive side contains VO^{2+} and VO_2^+. The latter can be respectively abbreviated as V^{4+} and V^{5+}, owing to the oxidation state of vanadium in those ions. During battery operation, both electrolytes are pumped from the reservoirs to an electrochemical cell (or stack of cells), where the redox reactions occur. An ion-exchange membrane within the cell separates the two electrolytes, allowing the electric circuit to close while preventing their direct interaction. The outlets of each half-cell are connected to their respective reservoirs, completing the hydraulic circuit. Fig. 1 provides a schematic representation of a standard VFB system. Note that the figure also includes two auxiliary cells for half-cell voltage monitoring, whose function will be discussed in detail in Section 3.

The primary electrochemical reactions occurring at the surface of the electrodes are as follows:

At the negative electrode: $$V^{2+} \underset{charge}{\overset{discharge}{\rightleftharpoons}} V^{3+} + e^-$$

At the positive electrode: $$VO_2^+ + 2H^+ + e^- \underset{charge}{\overset{discharge}{\rightleftharpoons}} VO^{2+} + H_2O$$

In addition to these reactions, a VFB system may experience other side reactions occurring at a significantly lower rate. These reactions

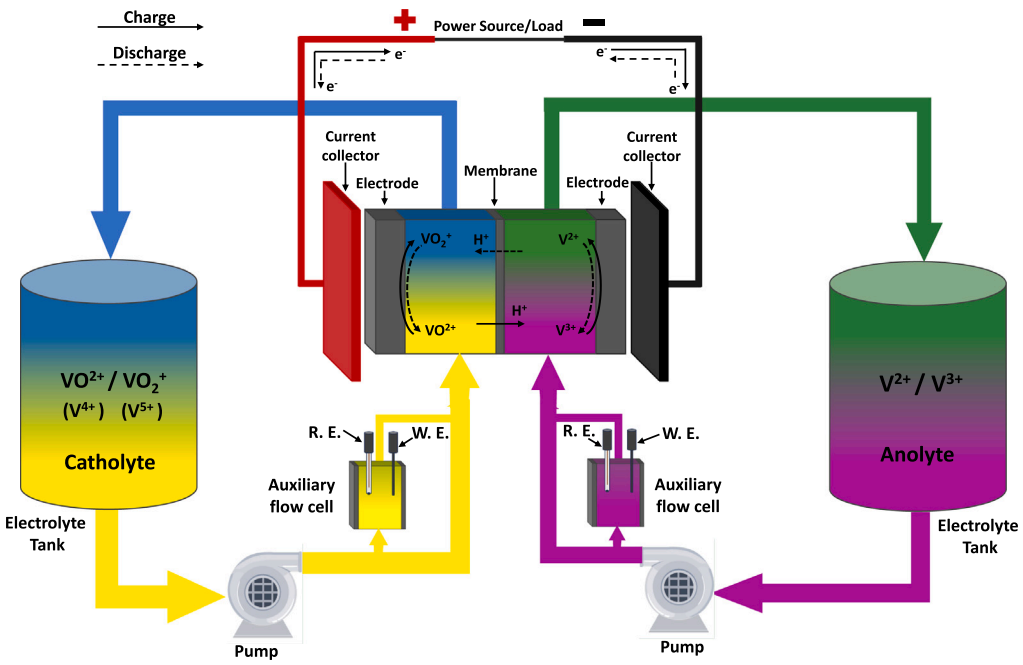

Fig. 1. Schematic of a single-cell vanadium flow battery system, including two auxiliary flow cells for half-cell voltage monitoring. R.E. and W.E. stand for Reference and Working Electrode, respectively.

contribute to self-discharge and, more significantly, lead to an electrolyte imbalance, thereby diminishing the battery's charge capacity (Puleston et al., 2024; Nolte et al., 2021). The most common side reactions stem from the undesired crossover of vanadium species through the membrane. Typically, the molar flux of vanadium in one direction surpasses that in the other, creating an asymmetric crossover. This imbalance results in accumulation on one side and depletion on the other, causing what is termed as "concentration imbalance" (Cremoncini et al., 2023). While this condition reduces battery capacity, it can be rectified in a relatively simple manner, remixing the electrolytes and evenly splitting the resulting solution.

On the contrary, side reactions that cause a net oxidation (or reduction) of the electrolyte, modifying the ideal overall average oxidation state of +3.5, give rise to a condition known as "faradaic imbalance" (Nourani et al., 2019). This type of imbalance results in a capacity loss that requires more intricate chemical or electrochemical methods for restoration (Poli et al., 2021; Cremoncini et al., 2023). Examples of such reactions include the hydrogen evolution reaction at the negative electrode during charge operation and the air oxidation suffered by V^{2+} when the negative tank is not perfectly sealed (Jirabovornwisut and Arpornwichanop, 2019).

2.2. Complete model

Many models are available in the literature for describing the dynamics of vanadium species concentrations in VFBs systems. For control and estimation purposes, the most popular are lumped parameter models derived from Tang and Skyllas-Kazacos formulations (Tang et al., 2011), and its subsequent improvements (Li et al., 2021; Puleston et al., 2022). In particular, considering that the VFB is composed of two tanks and a stack of m cells that behave exactly the same, the following experimentally validated eigth-order model (Bogdanov et al., 2023) can be formulated:

For V^{2+}

$$\begin{cases} v_{c,n}\dfrac{dc_2^c}{dt} = \dfrac{q_n}{m}(c_2^t - c_2^c) - S(N_2 + N_4 + 2N_5) + \dfrac{I}{F} & \text{(1a)} \\ v_{t,n}\dfrac{dc_2^t}{dt} = q_n(c_2^c - c_2^t) - k_{ox}c_2^t & \text{(1b)} \end{cases}$$

For V^{3+}

$$\begin{cases} v_{c,n}\dfrac{dc_3^c}{dt} = \dfrac{q_n}{m}(c_3^t - c_3^c) - S(N_3 - 2N_4 - 3N_5) - \dfrac{I}{F} & \text{(2a)} \\ v_{t,n}\dfrac{dc_3^t}{dt} = q_n(c_3^c - c_3^t) + k_{ox}c_2^t & \text{(2b)} \end{cases}$$

For V^{4+}

$$\begin{cases} v_{c,p}\dfrac{dc_4^c}{dt} = \dfrac{q_p}{m}(c_4^t - c_4^c) - S(N_4 - 3N_2 - 2N_3) - \dfrac{I}{F} & \text{(3a)} \\ v_{t,p}\dfrac{dc_4^t}{dt} = q_p(c_4^c - c_4^t) & \text{(3b)} \end{cases}$$

For V^{5+}

$$\begin{cases} v_{c,p}\dfrac{dc_5^c}{dt} = \dfrac{q_p}{m}(c_5^t - c_5^c) - S(N_5 + 2N_2 + N_3) + \dfrac{I}{F} & \text{(4a)} \\ v_{t,p}\dfrac{dc_5^t}{dt} = q_p(c_5^c - c_5^t) & \text{(4b)} \end{cases}$$

where c_i are the vanadium species concentrations (i indicates the vanadium oxidation state), v is the tank/half-cell volumes, q is the flow rate, m is the number of cells in the stack I is the stack current (considered positive in charge operation), F is the Faraday constant, S is the membrane area, N_i is the molar flux of species i through the membrane, and k_{ox} is a factor used to represent possible V^{2+} oxidation in the negative electrolyte tank. The subscripts and superscripts c and t stand for cells and tanks, while n and p refer to the negative and positive side of the system, respectively.

The ideal cell voltage, also referred to as Open Circuit Voltage (OCV), depends on the active species concentrations through the Nernst equation (Puleston et al., 2022; Zhang et al., 2015):

$$E_{cell}^{oc} = E^{\theta} + \frac{RT}{F}\ln\left(\frac{c_2^c c_5^c}{c_3^c c_4^c}\right), \quad (5)$$

where R is the ideal gas constant, and E^{θ} is the formal potential, that lumps the standard cell potential and other constant terms, such as activity coefficients and proton concentrations.

$$\mathbf{A_1} = \begin{bmatrix} (m\,v_c)^{-1} & 0 & 0 & 0 & (m\,v_c)^{-1} & 0 & 0 & 0 \\ 0 & -(m\,v_c)^{-1} & 0 & 0 & 0 & (m\,v_c)^{-1} & 0 & 0 \\ 0 & 0 & -(m\,v_c)^{-1} & 0 & 0 & 0 & (m\,v_c)^{-1} & 0 \\ 0 & 0 & 0 & -(m\,v_c)^{-1} & 0 & 0 & 0 & (m\,v_c)^{-1} \\ v_t^{-1} & 0 & 0 & 0 & -v_t^{-1} & 0 & 0 & 0 \\ 0 & v_t^{-1} & 0 & 0 & 0 & -v_t^{-1} & 0 & 0 \\ 0 & 0 & v_t^{-1} & 0 & 0 & 0 & -v_t^{-1} & 0 \\ 0 & 0 & 0 & v_t^{-1} & 0 & 0 & 0 & -v_t^{-1} \end{bmatrix},$$

$$\mathbf{A_2} = \begin{bmatrix} -k_2 & 0 & -k_4 & -2k_5 & 0 & 0 & 0 & 0 \\ 0 & -k_3 & 2k_4 & 3k_5 & 0 & 0 & 0 & 0 \\ 3k_2 & 2k_3 & -k_4 & 0 & 0 & 0 & 0 & 0 \\ -2k_2 & -k_3 & 0 & -k_5 & 0 & 0 & 0 & 0 \\ 0 & 0 & 0 & 0 & -k_{ox}\frac{d}{S}\frac{v_t}{v_c} & 0 & 0 & 0 \\ 0 & 0 & 0 & 0 & k_{ox}\frac{d}{S}\frac{v_t}{v_c} & 0 & 0 & 0 \\ 0 & 0 & 0 & 0 & 0 & 0 & 0 & 0 \\ 0 & 0 & 0 & 0 & 0 & 0 & 0 & 0 \end{bmatrix},$$

Box I.

Naturally, when an external current is applied, the voltage will deviate from the ideal E^{oc}_{cell} as a result of a series of overpotentials. However, in VFBs, it is a common practice to place an auxiliary open circuit cell that allows to obtain a direct measure of E^{oc}_{cell} (Nolte et al., 2021). Alternatively, if the overpotential parameters are well characterised, it is possible to estimate E^{oc}_{cell} from the terminal voltage (Fornaro et al., 2022). As a result, the remainder of this paper will assume that E^{oc}_{cell} can be directly measured.

2.3. State-space model

The electrochemical model presented in the previous subsections can be expressed more concisely in a state-space representation, which will facilitate the observer design process. Without loss of generality and to avoid unnecessarily lengthy expressions, it will be assumed that the flow rates as well as the tanks and half-cell volumes are the same in both sides of the system. If that is not the case, independent values for these variables can be defined in the model. In addition, it is assumed a linear diffusion law to represent vanadium crossover, which in general shows a good agreement with the experimental data (Bogdanov et al., 2023). The resulting model is as follows:

$$\begin{cases} \dot{\mathbf{x}} := f(\mathbf{x}) = q\mathbf{A_1}\mathbf{x} + \dfrac{S}{d\,v_c}\mathbf{A_2}\mathbf{x} + \dfrac{1}{F v_c}\mathbf{b}I & \text{(6a)} \\ y := h(\mathbf{x}) = E^{\theta} + \dfrac{RT}{F}\ln\left(\dfrac{x_1\,x_4}{x_2\,x_3}\right), & \text{(6b)} \end{cases}$$

where $\mathbf{x}$ is the concentrations vector $\mathbf{x} := [\mathbf{x_c}; \mathbf{x_t}] := [c^c_2\ c^c_3\ c^c_4\ c^c_5\ c^t_2\ c^t_3\ c^t_4\ c^t_5]^\top$; $\mathbf{A_1}$ describes the transport of vanadium between tanks and cells; $\mathbf{A_2}$ represents the side reaction dynamics, i.e., crossover and vanadium oxidation; $\mathbf{b} = [1\ 1\ 1\ 1\ 0\ 0\ 0\ 0]^\top$ represents the effect of the electric current, i.e., the main electrochemical reactions; and S and d are the membrane area and thickness, respectively. The expressions for $\mathbf{A_1}$ and $\mathbf{A_2}$ are given in Box I, where k_i is the membrane permeability coefficient of the species V^{i+}.

In this work, given that the side reactions proceed at a much slower time-scale than the main electrochemical processes, we make the assumption $\mathbf{A_2} = \mathbf{0}$ for the observer design in Section 4. The correction term of the observer will allow to compensate this slight discrepancy in the model, allowing to track their effects, particularly the electrolyte imbalance. The complete model considering crossover and side reactions will be utilised as ground truth for simulating the real plant in Section 5.

3. Problem formulation

This section formally states the specific objectives that the observer must achieve. Subsequently, the feasibility of designing such observer is discussed by means of an observability analysis. Finally, it is demonstrated that the utilisation of two half-cell voltage measurements is sufficient to attain full observability of the system.

3.1. Observer objectives

The primary objective is to design an observer capable of estimating, in real time, the concentrations of the four vanadium species present in a VFB system, relying only on voltage and current measurements. That is,

$$\lim_{t\to\infty} |\mathbf{x}(t) - \hat{\mathbf{x}}(t)| = \mathbf{0}, \tag{7}$$

where $\mathbf{x}$ is the concentrations vector and $\hat{\mathbf{x}}$ is the estimation generated by the observer. Naturally, in the presence of sensor noise and model uncertainty, achieving the objective outlined in (7) becomes unattainable. Instead, we can ensure practical convergence, denoted as $\lim_{t\to\infty} |\hat{\mathbf{x}}(t) - \mathbf{x}(t)| \leq \varepsilon$, where ε is a positive constant. Coherently, the observer must minimise the constant ε, that is, the impact of sensor noise and parametric uncertainty on the quality of the estimation.

Specifically, this work addresses two significant challenges. Firstly, the observer should adequately operate under electrolyte imbalance conditions. Since VFB tend to suffer from both concentration and faradaic imbalances after extended operation, the removal of the "balanced electrolytes" hypothesis common from the VFB estimation literature results of utmost importance for almost every VFB system. Secondly, the observer needs to differentiate between the concentrations of tanks and cells, without imposing the usual hypothesis of a "very high flow rate" that equalises these concentrations. This distinction becomes particularly relevant in those applications where the flow rate is being regulated, either to optimise the energy efficiency, or to mitigate the degradation of certain battery components.

Moreover, the observer needs to estimate the system concentrations even when no prior information regarding the system state is available. That is, the observer initial conditions may be arbitrarily far from the real ones without affecting the stability and convergence of the algorithm. In addition, there is no side information regarding the VFB level of imbalance, e.g., the overall average oxidation state of the system is unknown.

3.2. Observability study: additional sensors justification

Prior to any observer design, it is crucial to analyse if the estimation problem formulated in Section 3.1 is actually solvable. More precisely, we need to study if the measured signal, y, contains enough information to infer the values of the unmeasured concentrations. In the control community, this process is known as an observability analysis.

Previous results have proven that just using the open-circuit voltage results insufficient to achieve full observability (Jienkulsawad et al., 2020; Yu et al., 2014). More precisely, in Puleston et al. (2023), it has been shown that this is because every trajectory in the output voltage could correspond to four different (non-converging) trajectories in the concentrations space, thus making the system non-observable.

In this work, we propose to overcome this limitation with the inclusion of two reference electrodes that allow to have independent voltage measurements for each side of the system. Consequently, the traditional OCV measurement is replaced by two half-cell voltage measurements, each responsive to a single vanadium couple (Haisch et al., 2020; Nolte et al., 2021). Specifically, the voltage measurement corresponding to the negative side of the system will be sensitive only to the concentrations of V^{2+} and V^{3+} while the one of the positive side will be sensitive to the concentrations of V^{4+} and V^{5+}. To obtain these measurements, an auxiliary cell is connected to the outlet of each electrolyte tank. Each auxiliary cell is equipped with two electrodes: a reference electrode (such as Ag/AgCl or $Hg/HgSO_4$) with a constant potential; and a glassy carbon rod that is exposed to the vanadium electrolyte, as working electrode. The potential difference between the working and reference electrode constitutes the so-called half cell voltage. Note that, since reference electrodes may suffer from some potential drift after extended operation, it is recommended to periodically recalibrate them to maintain accurate potential values (Ressel et al., 2018). As anticipated in Section 2, a schematic representation of the proposed setup, based on the configuration described in Haisch et al. (2020), is shown in Fig. 1.

Accordingly, the measured voltages between the reference and working electrodes will be (Nolte et al., 2021; Haisch et al., 2020):

$$\text{Negative side:} \quad E_{neg} = E^0_{neg} + \frac{RT}{F}\ln\left(\frac{c_3^t}{c_2^t}\frac{\gamma_3}{\gamma_2}\right) \tag{8a}$$

$$\text{Positive side:} \quad E_{pos} = E^0_{pos} + \frac{RT}{F}\ln\left(\frac{c_5^t c_H^2}{c_4^t}\frac{\gamma_5\gamma_H^2}{\gamma_4}\right), \tag{8b}$$

where E^0_{neg} and E^0_{pos} are the standard potentials of the working electrode against the reference electrodes in the positive and negative side of the system, respectively, and γ_i are the activity coefficient of species i. Combining the activity coefficients with the standard potentials, the formal potentials E^θ_{neg} and E^θ_{pos} are obtained (Li et al., 2021; Haisch et al., 2020). Then, subtracting from (8) all the constant terms and rearranging, the following auxiliary outputs can be derived:

$$\text{Negative side:} \quad \bar{y}_1 = -\frac{F}{RT}(E_{neg} - E^\theta_{neg}) = \ln\left(\frac{c_2^t}{c_3^t}\right) \tag{9a}$$

$$\text{Positive side:} \quad \bar{y}_2 = \frac{F}{RT}(E_{pos} - E^\theta_{pos}) = \ln\left(\frac{c_5^t}{c_4^t}\right). \tag{9b}$$

Note that for obtaining (9b), the H^+ concentration is assumed to be approximately constant and hence lumped with the formal potential E^θ_{pos}. This is a typical assumption in the literature, given the initially high acid concentration in the electrolyte (Clemente et al., 2023; Zhang et al., 2015; Yu et al., 2014).

In the following, we will show that by using half-cell measurements we recover the observability of the system. We remark that observability analysis of a high-order system is very complex in nonlinear systems given the lack of a systematic procedure for doing so. In this case, the observability can be studied for a simplified version of the model, assuming that the flow rate is sufficiently large to equalise the tanks and cells concentrations and that the side reaction dynamics are negligible in short time periods ($\mathbf{A_2} = \mathbf{0}$). We can make such an assumption since even in those cases when the "very high flow rate condition" is not satisfied, the tanks-cells dynamics are stable. This is, the observability of the simplified model (10) implies, at least, the detectability of the complete model (6). More details on this stability of the tank-cells dynamics can be found in Section 4.1. More precisely, under high flow rates assumption, the VFB model reduces to:

$$\begin{cases} \dot{\bar{\mathbf{x}}} := f(\bar{\mathbf{x}}) = \mathbf{b}I & \text{(10a)} \\ \bar{y}_1 := h_1(\bar{\mathbf{x}}) = \ln\left(\dfrac{\bar{x}_1}{\bar{x}_2}\right) & \text{(10b)} \\ \bar{y}_2 := h_2(\bar{\mathbf{x}}) = \ln\left(\dfrac{\bar{x}_4}{\bar{x}_3}\right), & \text{(10c)} \end{cases}$$

where $\bar{\mathbf{x}} = [\bar{x}_1\ \bar{x}_2\ \bar{x}_3\ \bar{x}_4]^\top = [c_2\ c_3\ c_4\ c_5]^\top$, $\mathbf{b} = [k\ \ -k\ \ -k\ \ k]^\top$, with $k = \frac{m}{F(v_t + m v_e)}$. By looking at (10), it can be appreciated that the ratio between the vanadium species in each side of the system can be obtained directly by computing the exponential of the outputs $\bar{y}_1$ and $\bar{y}_2$. Nevertheless, because of crossover and other undesired phenomena, the total concentration of vanadium may change after extended operation. Therefore, determining the absolute concentration of individual vanadium species based solely on a single instance of these measurements is unfeasible (Neyhouse et al., 2021; Jienkulsawad et al., 2020). On the contrary, designing an observer that utilises the full trajectory of the signals $\bar{y}_1$ and $\bar{y}_2$ ends up being a much more robust solution.

The observability of the system (10) can be evaluated by means of the observability map, i.e., the vector of successive time derivatives of the outputs, up to the order σ (Hermann and Krener, 1977). Since we have two outputs and four states, it is sufficient to compute only the first order derivative for each of the outputs ($\sigma = 1$), as follows:

$$O(\bar{\mathbf{x}}) := \begin{bmatrix} \bar{y}_1 \\ \dot{\bar{y}}_1 \\ \bar{y}_2 \\ \dot{\bar{y}}_2 \end{bmatrix} = \begin{bmatrix} \ln(\bar{x}_1) - \ln(\bar{x}_2) \\ \frac{kI}{\bar{x}_1} + \frac{kI}{\bar{x}_2} \\ \ln(\bar{x}_4) - \ln(\bar{x}_3) \\ \frac{kI}{\bar{x}_4} + \frac{kI}{\bar{x}_3} \end{bmatrix}. \tag{11}$$

If the observability map (11) is injective, then, the system (10) will be observable (Hermann and Krener, 1977). Indeed, the Jacobian matrix for $O(\bar{\mathbf{x}})$ is:

$$J(\bar{\mathbf{x}}) := \frac{\partial O(\bar{\mathbf{x}})}{\partial \bar{\mathbf{x}}} = \begin{bmatrix} \frac{1}{\bar{x}_1} & -\frac{1}{\bar{x}_2} & 0 & 0 \\ -\frac{kI}{\bar{x}_1^2} & -\frac{kI}{\bar{x}_2^2} & 0 & 0 \\ 0 & 0 & -\frac{1}{\bar{x}_3} & \frac{1}{\bar{x}_4} \\ 0 & 0 & -\frac{kI}{\bar{x}_3^2} & -\frac{kI}{\bar{x}_4^2} \end{bmatrix}, \tag{12}$$

Then, if the Jacobian matrix $J(\bar{\mathbf{x}})$ is full rank, the observability map (11) is injective. Specifically, the determinant of (12) is

$$\mathrm{Det}(J(\bar{\mathbf{x}})) = -(kI)^2 \frac{\bar{x}_1\bar{x}_3 + \bar{x}_1\bar{x}_4 + \bar{x}_2\bar{x}_3 + \bar{x}_2\bar{x}_4}{\bar{x}_1^2\,\bar{x}_2^2\,\bar{x}_3^2\,\bar{x}_4^2}. \tag{13}$$

Since the concentrations must be positive ($\bar{\mathbf{x}} > 0$), it will hold that $\mathrm{Det}(J(\bar{\mathbf{x}})) \neq 0$ as long as $I \neq 0$. Therefore, the observability map (11) is injective and the system (10) will be observable as long as $I \neq 0$. Conversely, it will become non-observable when $I = 0$.

In summary, by means of the half-cell measurements and from the theoretical point of view, it will be possible to reconstruct the concentrations state as long as the current is non-zero. On the contrary, by just using the open-circuit voltage as the measured signal it is not possible to uniquely reconstruct the concentrations state.

4. Methodology

This section presents the methodology for designing the proposed observer to meet the objectives established in Section 3. The measured outputs that drive the estimation process are the half-cell voltage

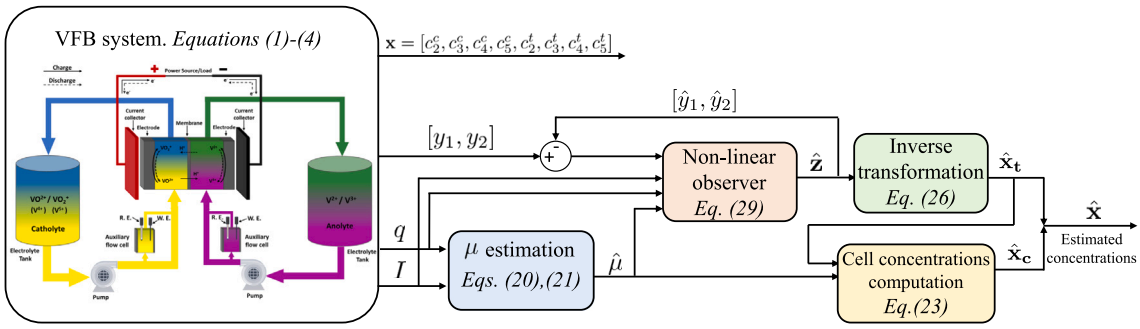

Fig. 2. Schematic flowchart of the designed observer. The algorithm utilises the current, flow rates and half-cell voltages as inputs, and provides estimates of the concentrations in tanks and cells of the four vanadium species.

measurements $\bar{y}_1$ and $\bar{y}_2$, as expressed in (9). To facilitate the comprehension of this section, an schematic diagram of the proposal is presented in Fig. 2. We remark that some of the variables and equations that appear in the figure will be introduced and formulated later over the course of this section.

4.1. Model rearrangement: cell dynamics separation

The objective of this subsection is to rewrite system (6) in a way that it decouples tanks and cells dynamics, aiming to obtain a reduced order model that is more convenient for observer design purposes. To avoid unnecessary repetition, the detailed procedure followed to make this separation is explained only for the negative side of the VFB system, being the procedure for the positive side completely equivalent.

Accordingly, the dynamics for the negative side of the system are:

$$\begin{cases} \dot{x}_1 = \dfrac{q_n}{m\,v_c}(x_5 - x_1) + \dfrac{I}{F v_c} & \text{(14a)} \\ \dot{x}_2 = \dfrac{q_n}{m\,v_c}(x_6 - x_2) - \dfrac{I}{F v_c} & \text{(14b)} \\ \dot{x}_5 = \dfrac{q_n}{v_t}(x_1 - x_5) & \text{(14c)} \\ \dot{x}_6 = \dfrac{q_n}{v_t}(x_6 - x_2) & \text{(14d)} \end{cases}$$

To separate the cell and tank dynamics we make the observation that the dynamics of the difference between cell and tank concentration is stable. Therefore, we can trivially design an observer for this difference. We define $\mu_1 := x_1 - x_5$, i.e., the difference between V^{2+} concentration in the cells and the tank. Its dynamics are the following:

$$\dot{\mu}_1 = \dot{x}_1 - \dot{x}_5 = -q_n\left(\frac{1}{m\,v_c} + \frac{1}{v_t}\right)\mu_1 + \frac{I}{F v_c}. \tag{15}$$

Let us consider a trivial observer for μ_1 that consists of a copy of its dynamics, i.e.,:

$$\dot{\hat{\mu}}_1 = \dot{\hat{x}}_1 - \dot{\hat{x}}_5 = -q_n\left(\frac{1}{m\,v_c} + \frac{1}{v_t}\right)\hat{\mu}_1 + \frac{I}{F v_c}. \tag{16}$$

Defining the estimation error as $\tilde{\mu}_1 := \mu_1 - \hat{\mu}_1$, the resulting error dynamics are:

$$\begin{aligned} \dot{\tilde{\mu}}_1 = \dot{\mu}_1 - \dot{\hat{\mu}}_1 = &\left[-q_n\left(\frac{1}{m\,v_c} + \frac{1}{v_t}\right)\mu_1 + \frac{I}{F v_c}\right] \\ &- \left[-q_n\left(\frac{1}{m\,v_c} + \frac{1}{v_t}\right)\hat{\mu}_1 + \frac{I}{F v_c}\right] = \\ = &- q_n\left(\frac{1}{m\,v_c} + \frac{1}{v_t}\right)\tilde{\mu}_1. \end{aligned} \tag{17}$$

Since $q_n, v_c, v_t > 0$, Eq. (17) corresponds to a stable dynamic,[1] which implies that the error in the estimation of μ_1 will converge to zero regardless of the initial guess for $\hat{\mu}_1$, i.e., $\lim_{t\to\infty} |\mu_1(t) - \hat{\mu}_1(t)| = 0$. In addition, it can be noted that the electrolyte residence time in the stack ($m\,v_c/q_n$) constitutes an upper bound for the time-constant that defines the convergence rate of (17). Then, since the residence time in the cells is typically very short (Bogdanov et al., 2023), the convergence time of (16) will be very fast.

Similarly, we define $\mu_2 := x_2 - x_6$, whose dynamics are given by:

$$\dot{\mu}_2 = \dot{x}_2 - \dot{x}_6 = -q_n\left(\frac{1}{m\,v_c} + \frac{1}{v_t}\right)\mu_2 - \frac{I}{F v_c}. \tag{18}$$

Considering for μ_2 a trivial observer analogous to (16), and defining $\tilde{\mu}_2 := \mu_2 - \hat{\mu}_2$, the resulting error dynamics are:

$$\dot{\tilde{\mu}}_2 = \dot{\mu}_2 - \dot{\hat{\mu}}_2 = -q_n\left(\frac{1}{m\,v_c} + \frac{1}{v_t}\right)\tilde{\mu}_2. \tag{19}$$

Again, Eq. (19) implies that the error in the estimation of μ_2 will also converge to zero regardless of the initial guess for $\hat{\mu}_2$, i.e., $\lim_{t\to\infty} |\mu_2(t) - \hat{\mu}_2(t)| = 0$. Additionally, it holds that if $\hat{\mu}_2(0) = -\hat{\mu}_1(0)$, then $\hat{\mu}_2(t) = -\hat{\mu}_1(t)$ for all time $t \geq 0$ (see the proof in Appendix A). Therefore, imposing $\hat{\mu}_2(0) = -\hat{\mu}_1(0)$, a single variable can be defined $\hat{\mu}_n := \hat{\mu}_1 = -\hat{\mu}_2$. That is, we can design an observer for μ_1 and μ_2 as

$$\dot{\hat{\mu}}_n = -q_n\left(\frac{1}{m\,v_c} + \frac{1}{v_t}\right)\hat{\mu}_n + \frac{I}{F v_c}, \quad \hat{\mu}_1 = \hat{\mu}_n, \quad \hat{\mu}_2 = -\hat{\mu}_n. \tag{20}$$

As anticipated, the existing symmetry in the VFB model allows to follow the same procedure for the positive side of the system, resulting in an equivalent set of equations. The observer for μ_p results:

$$\dot{\hat{\mu}}_p = -q_p\left(\frac{1}{m\,v_c} + \frac{1}{v_t}\right)\hat{\mu}_p + \frac{I}{F v_c}, \quad \hat{\mu}_3 = -\hat{\mu}_p, \quad \hat{\mu}_4 = \hat{\mu}_p. \tag{21}$$

Consequently, the tanks concentration dynamics can be expressed in terms of μ_n and μ_p as follows:

$$\dot{\mathbf{x}}_t = \begin{bmatrix} \dot{x}_5 \\ \dot{x}_6 \\ \dot{x}_7 \\ \dot{x}_8 \end{bmatrix} = \frac{1}{v_t}\begin{bmatrix} q_n\,\mu_1 \\ q_n\,\mu_2 \\ q_p\,\mu_3 \\ q_p\,\mu_4 \end{bmatrix} = \frac{1}{v_t}\begin{bmatrix} q_n\,\mu_n \\ -q_n\,\mu_n \\ -q_p\,\mu_p \\ q_p\,\mu_p \end{bmatrix}. \tag{22}$$

In summary, the procedure followed in this subsection has allowed to transform the tanks dynamics into a function of the variables μ_n and μ_p which are, initially unknown, but can be accurately estimated by means of (20) and (21). Therefore, it is possible to consider μ_n and μ_p as known inputs and, accordingly, design an observer only for the tanks concentrations, as will be done in the following subsections. As for the cell concentrations, once the estimates for the tanks concentrations are

[1] In the case of a varying $q_n(t)$, (17) results in a LTV system, whose stability condition is $\lim_{t\to\infty} \int_0^t q_n(s)ds = \infty$. Since, the flow rate must be kept high enough and positive to provide the stack of enough reactants to sustain the electrochemical reaction, this condition will be satisfied in every practical application.

available, they can be directly obtained from:

$$\hat{\mathbf{x}}_c = \begin{bmatrix} \hat{x}_1 \\ \hat{x}_2 \\ \hat{x}_3 \\ \hat{x}_4 \end{bmatrix} = \begin{bmatrix} \hat{x}_5 + \hat{\mu}_n \\ \hat{x}_6 - \hat{\mu}_n \\ \hat{x}_7 - \hat{\mu}_p \\ \hat{x}_8 + \hat{\mu}_p \end{bmatrix}. \tag{23}$$

4.2. Model rearrangement: coordinates change

The procedure followed in the previous subsection has substantially improved the structure of the observation problem by eliminating the explicit dependence of the tanks dynamics on the cell concentrations, as appreciated in (22). In this section, we propose a coordinate change to bring the system (22) into a more convenient form for observer design. The objective of this transformation is twofold. Firstly, it resolves the numerical and stability issues that may occur when the original states approach zero. Effectively, when the reactant concentrations tend to zero, the fractional terms of (12) tend to infinity, resulting in a nearly singular Jacobian matrix. Secondly, it brings the system dynamics into a triangular form which is well-suited for the design of an observer (Bernard et al., 2022).

For simplicity, we rewrite (22) by defining $\mathbf{u} := [u_n \ , \ u_p]^\top := [\frac{q_n}{v_t}\mu_n \ , \ \frac{q_p}{v_t}\mu_p]^\top$, and we eliminate the logarithms from the outputs by imposing $[y_1 \ y_2] := [e^{\bar{y}_1} \ e^{\bar{y}_2}]$. Then, the resulting tanks dynamics are:

$$\begin{cases} \dot{\mathbf{x}}_\mathbf{t} = [u_n \ -u_n \ -u_p \ u_p]^\top & \text{(24a)} \\ y_1 = \dfrac{x_5}{x_6} & \text{(24b)} \\ y_2 = \dfrac{x_8}{x_7} & \text{(24c)} \end{cases}$$

Taking the concentration ratios and the inverse of the total vanadium concentration in each side of the system as new states, the following transformation is defined:

$$\mathbf{z} := \boldsymbol{\Phi}(\mathbf{x}_\mathbf{t}) = \begin{bmatrix} \frac{x_5}{x_6} \\ \frac{1}{x_5+x_6} \\ \frac{x_8}{x_7} \\ \frac{1}{x_7+x_8} \end{bmatrix}. \tag{25}$$

The inverse transformation results:

$$\mathbf{x}_\mathbf{t} := \boldsymbol{\Phi}^{-1}(\mathbf{z}) = \begin{bmatrix} \frac{z_1}{z_2(1+z_1)} \\ \frac{1}{z_2(1+z_1)} \\ \frac{1}{z_4(1+z_3)} \\ \frac{z_3}{z_4(1+z_3)} \end{bmatrix}. \tag{26}$$

The dynamics of the transformed system are:

$$\begin{cases} \dot{\mathbf{z}} := \begin{bmatrix} \dot{z_1} \\ \dot{z_2} \\ \dot{z_3} \\ \dot{z_4} \end{bmatrix} = \mathbf{f}(\mathbf{z}, \mathbf{u}) = \begin{bmatrix} u_n z_2 (1+z_1)^2 \\ 0 \\ u_p z_4 (1+z_3)^2 \\ 0 \end{bmatrix} & \text{(27a)} \\ y_1 = z_1 & \text{(27b)} \\ y_2 = z_3 & \text{(27c)} \end{cases}$$

Working on the new $\mathbf{z}$ coordinates in (27) presents a set of advantages relative to the original coordinates in (22). First, it is made explicit there is a time-scale separation between the total vanadium concentration in each side of the VFB and the concentration ratio, since $\dot{z}_2 = \dot{z}_4 = 0$. Second, in the new coordinates, the measured output is linear. This fact is crucial to simplify the observer design process (Bernard et al., 2022). Finally, the state estimation problem becomes well-posed in the new coordinates. More precisely, the Jacobian of the observability map in these new coordinates is:

$$J(\mathbf{z}) = \begin{bmatrix} 1 & 0 & 0 & 0 \\ 2u_n(1+z_1)z_2 & u_n(1+z_1)^2 & 0 & 0 \\ 0 & 0 & 1 & 0 \\ 0 & 0 & 2u_p(1+z_3)z_4 & u_p(1+z_3)^2 \end{bmatrix}, \tag{28}$$

which no longer loses rank when $z_i \to 0$. Therefore, since $z_i > 0$ we now have a well-posed estimation problem for any value of the VFB state and observer state.

We highlight that we can still lose rank when $I = 0$. Indeed, changing the coordinates cannot modify the fact that the system is not observable when $I = 0$, nonetheless, it can make the estimation problem well-posed from a numerical point of view.

4.3. Observer dynamics

The following observer is proposed for the system (27):

$$\dot{\hat{\mathbf{z}}} = \mathbf{f}(\hat{\mathbf{z}}, \mathbf{u}) + g(\hat{\mathbf{z}}, \mathbf{y}, \mathbf{u}) + \mathbf{M}(\hat{\mathbf{z}}), \tag{29}$$

where $\mathbf{f}(\hat{\mathbf{z}}, \mathbf{u})$ is a copy of the system dynamics presented in (27a), $\mathbf{g}(\hat{\mathbf{z}}, \mathbf{y}, \mathbf{u})$ is the correction term, and $\mathbf{M}(\hat{\mathbf{z}})$ is a factor that modifies the observer dynamics to preserve the estimates in a predefined set (Astolfi et al., 2022). The detailed proof of the observer global stability is available in Appendix B.

The expression for the correction term is the following:

$$g(\hat{\mathbf{z}}, \mathbf{y}, \mathbf{u}) = \begin{bmatrix} l\lambda_{1,n}[y_1 - \hat{z}_1] \\ l\lambda_{2,n}(u_n)[y_1 - \hat{z}_1] \\ l\lambda_{1,p}[y_2 - \hat{z}_3] \\ l\lambda_{2,p}\lambda_{2,n}(u_p)[y_2 - \hat{z}_3] \end{bmatrix}, \tag{30}$$

where l is a large enough positive constant ($l \geq 1$); $\lambda_{1,j} > 3\bar{u}(1+\bar{z}_1)^2$, where $\bar{u}_j$ is an upper bound for the input amplitude, $\bar{z}_j$ is an upper bound for the concentration ratios, and $\lambda_{2,j}(u_j) = \lambda_{1,j} \ \mathrm{sgn}(u_j)$, with $j \in \{n, p\}$.

The expression for the factor $\mathbf{M}(\hat{\mathbf{z}})$ is:

$$\mathbf{M}(\hat{\mathbf{z}}) = -\gamma \mathbf{P}^{-1}(\mathbf{u}) \frac{\partial \mathbf{r}(\hat{\mathbf{z}})}{\partial \hat{\mathbf{z}}} \mathbf{r}(\hat{\mathbf{z}}), \tag{31}$$

where γ is a large enough positive constant; $\mathbf{r}(\hat{\mathbf{z}}) = [r_1 \ r_2 \ r_3 \ r_4]^\top$, being $r_i = (\max\{\underline{z}_i - \hat{z}_i \ ; \ 0\})^2 + (\max\{\hat{z}_i - \bar{z}_i \ ; \ 0\})^2$, with $\underline{z}_i$ and $\bar{z}_i$ predefined lower and upper bounds for z_i, based on physics constraints; and $\mathbf{P}(\mathbf{u})$ is the matrix:

$$\mathbf{P}(\mathbf{u}) = \begin{bmatrix} 8 & -\mathrm{sgn}(u_n) & 0 & 0 \\ -\mathrm{sgn}(u_n) & 1 & 0 & 0 \\ 0 & 0 & 8 & -\mathrm{sgn}(u_p) \\ 0 & 0 & -\mathrm{sgn}(u_p) & 1 \end{bmatrix}. \tag{32}$$

In the proposed observer, the correction term (30) guarantees the convergence of the estimated states, $\hat{\mathbf{z}}$, to the real ones, $\mathbf{z}$, regardless of the observer initial condition. Since the observer operates in the $\mathbf{z}$-coordinates, the vanadium species concentrations are reconstructed by means of the inverse transformation (26), $\hat{\mathbf{x}}_\mathbf{t} = \boldsymbol{\Phi}^{-1}(\hat{\mathbf{z}})$. On the other hand, the factor $\mathbf{M}(\hat{\mathbf{z}})$, allows to apply the physical knowledge of the system. By imposing realistic constraints to the concentration's ratio and the total concentration, the transient behaviour of the algorithm is significantly enhanced. Specifically, the convergence of the algorithm is accelerated, and the possibility of obtaining estimates lacking physical sense, such as a negative concentration, is eliminated. It is important to highlight that, unlike just saturating the states of the observer, the factor $\mathbf{M}(\hat{\mathbf{z}})$ is integrated within the dynamics of the observer and, consequently, does not negatively affect the convergence, stability and robustness of the algorithm (Astolfi et al., 2022).

Furthermore, it is possible to show that when the system is in a non-observable region (i.e., for $\mathbf{u} = 0$), the observer estimation will not diverge. To see this fact, notice that by taking $\mathbf{u} = 0$ and $\mathbf{M}(\hat{\mathbf{z}}) = \mathbf{0}$, the

dynamics for the system (27) are given by $\dot{\mathbf{z}} = [0\ 0\ 0\ 0]^\top$. Coherently, (29) becomes

$$\dot{\hat{\mathbf{z}}} = \begin{bmatrix} \lambda_{1,n}(z_1 - \hat{z}_1) \\ 0 \\ \lambda_{1,p}(z_3 - \hat{z}_3) \\ 0 \end{bmatrix}. \tag{33}$$

The estimation error ($\tilde{\mathbf{z}} := \mathbf{z} - \hat{\mathbf{z}}$) dynamics result:

$$\dot{\tilde{\mathbf{z}}} = \dot{\mathbf{z}} - \dot{\hat{\mathbf{z}}} = \begin{bmatrix} -\lambda_{1,n}\tilde{z}_1 \\ 0 \\ -\lambda_{1,p}\tilde{z}_3 \\ 0 \end{bmatrix}, \tag{34}$$

which implies that for $\mathbf{u} = 0$, the estimation error for z_1 and z_3 will decrease, while the error for z_2 and z_4 will remain constant, without diverging or causing stability issues for the observer. Eventually, when $\mathbf{u}$ ceases to be equal to zero, the convergence of the algorithm will resume.

4.4. Proposal summary

The steps involved in reconstructing the eight concentrations of the VFB system are outlined as follows (see Fig. 2):

1. The difference between tanks and cells concentrations, μ_n and μ_p, is estimated from current and flow rate measurements, by means of Eqs. (20) and (21).
2. The vanadium species concentration ratio and the inverse of the total concentration in each side of the system is estimated with the observer (29). To generate the estimates $\hat{\mathbf{z}}$, the observer utilises $\hat{\mu}_n$, $\hat{\mu}_p$, q_n, q_p, I, and the measured half-cell voltages as inputs.
3. The tanks concentrations are reconstructed by computing the inverse transformation (26): $\hat{\mathbf{x}}_\mathbf{t} = \boldsymbol{\Phi}^{-1}(\hat{\mathbf{z}})$.
4. The cell concentrations $\hat{\mathbf{x}}_\mathbf{c}$ are reconstructed from $\hat{\mu}_n$, $\hat{\mu}_p$ and the tanks concentrations using (23).

The tuning of the observer is simple and intuitive, since it requires a reduced number of parameters with a clear physical interpretation. These parameters are:

- $l > 1$ and $\gamma > 1$, sufficiently large positive constants.
- $\bar{u}$, an upper bound for the input amplitude ($\bar{u} > |u|$). It can be interpreted as the maximum rate of variation for the tanks concentrations, and can be approximated in terms of an upper bound for the current: $\bar{u} > \frac{m|I|}{F(v_t + m v_c)}$.
- $\lambda_{1,j}$ and $\lambda_{2,j}$, correction term gains defined as $\lambda_{1,j} > 3\bar{u}(1 + \bar{z}_1)^2$, $\lambda_{2,j}(u_j) = \lambda_{1,j}\ \mathrm{sgn}(u_j)$, with $u = \frac{q_j}{v_t}\mu_j$ and $j \in \{n, p\}$.
- The factors z_i and $\bar{z}_i$ from (31), predefined lower and upper bounds for z_i, based on physics constraints. For instance, for the concentrations ratios z_1 and z_3 a minimum and maximum limits of 0.05 and 20, respectively, could be set. On the other hand, for the total vanadium concentration, it can be assumed that the crossover can produce, at most, a change of a 50% with respect to the original vanadium concentration c_{v_0}, resulting in $\underline{z_2} = \underline{z_4} = \frac{1}{1.5 c_{v_0}}$ and $\bar{z}_2 = \bar{z}_4 = \frac{1}{0.5 c_{v_0}}$.

5. Results and discussion

This section presents a series of comprehensive simulations to illustrate the functioning of the proposed observer and assess its performance. The first set of simulations is intended to demonstrate the steps followed by the observer to reconstruct the complete concentrations state $\mathbf{x}$, in a typical charge–discharge cycling operation. In the following set, some particular cases are considered to highlight the observer capabilities dealing with challenging conditions, which include a varying flow rate and intervals of zero current. Finally, the importance of counting with reliable online concentrations estimates is exemplified with its use for determining the system's SoC and level of imbalance, and subsequently for the development of a flow rate modulation strategy.

To conduct the tests, the complete model presented in Eq. (6), which incorporates crossover and oxidation side reactions, is used as ground truth for simulating the real plant. Moreover, to assess the algorithm under realistic conditions, additive white noise with a peak-to-peak amplitude of a 1% of each signal is included in both voltages and current measures.

The sizing and physicochemical parameters of the VFB under study are presented in Table 1.

Table 1
VFB parameters. Coefficients k_i are taken from Cecchetti et al. (2023).

Parameter	Meaning	Value	Units
c_{v_0}	Original vanadium concentration	1.6	mol l^{-1}
d	Membrane thickness	$4 \cdot 10^{-4}$	m
F	Faraday constant	96 500	A s mol^{-1}
k_2	Permeability of V^{2+}	$1.30 \cdot 10^{-11}$	m^{2}s^{-1}
k_3	Permeability of V^{3+}	$1.25 \cdot 10^{-11}$	m^{2}s^{-1}
k_4	Permeability of V^{4+}	$3.81 \cdot 10^{-12}$	m^{2}s^{-1}
k_5	Permeability of V^{5+}	$3.10 \cdot 10^{-12}$	m^{2}s^{-1}
k_{ox}	Oxidation rate of V^{2+}	$3.1 \cdot 10^{-7}$	m^{3}s^{-1}
m	Number of cells	6	–
S	Membrane area	$2.5 \cdot 10^{-2}$	m^2
T	Temperature	298	K
v_t	Tank volume	4.8	l
v_c	Half-cell volume	0.0026	l

Table 2
Observer parameters.

Parameter	Meaning	Value	Units
l	Correction term parameter	5	–
γ	Flow redesign parameter	30	–
$\bar{u}$	Upper bound for $\lvert u\rvert$	$5 \cdot 10^{-4}$	mol l^{-1}s^{-1}
$\underline{z_1}$ ($\underline{z_3}$)	Lower bound for z_1 and z_3	0.05	–
$\bar{z}_1$ ($\bar{z}_3$)	Upper bound for z_1 and z_3	20	–
$\underline{z_2}$ ($\underline{z_4}$)	Lower bound for z_2 and z_4	0.41	1 mol^{-1}
$\bar{z}_2$ ($\bar{z}_4$)	Upper bound for z_2 and z_4	1.25	1 mol^{-1}

5.1. Concentrations state reconstruction

The first test comprises three successive charge–discharge cycles, with a State of Charge ranging from 15 to 85%. To assess the robustness of the observer under different current levels, its amplitude is set at 12 A (48 mA/cm^2) in the first cycle, 24 A (96 mA/cm^2) in the second cycle, and 50 A (200 mA/cm^2) in the third cycle, as representatives of a low, intermediate and high current density, respectively. The flow rate is set at 7.2 ml/s, 14.4 ml/s, and 30 ml/s, respectively. The initial concentrations of the system are $\mathbf{x}_0 = [0.4\ 0.7\ 0.55\ 1.25\ 0.7\ 0.7\ 0.55\ 1.25]^\top$, which represents a highly imbalanced condition, where the total vanadium concentration is 1.4 mol/l and 1.8 mol/l in the negative and positive side, respectively. To test the ability of the observer to converge without using previous information, its states are initialised very far from the real concentrations, with $\hat{\mathbf{x}}_0 = [1.2\ 1.2\ 1.2\ 1.2\ 0.4\ 0.4\ 0.4\ 0.4]^\top$. The observer is tuned following the steps summarised in Section 4.4, resulting in the parameters values presented in Table 2.

Fig. 3 depicts the complete procedure followed to reconstruct all the concentrations in the system. Firstly, Fig. 3a shows the estimation of the difference between tanks and cells concentrations, μ, which is obtained by means of (20) (step 1 of Section 4.4).[2] Note that, after

[2] Since the flow rate in both sides of the system is the same, the estimates $\hat{\mu}_n$ and $\hat{\mu}_p$ will be equal and, consequently, are represented as a single $\hat{\mu}$.

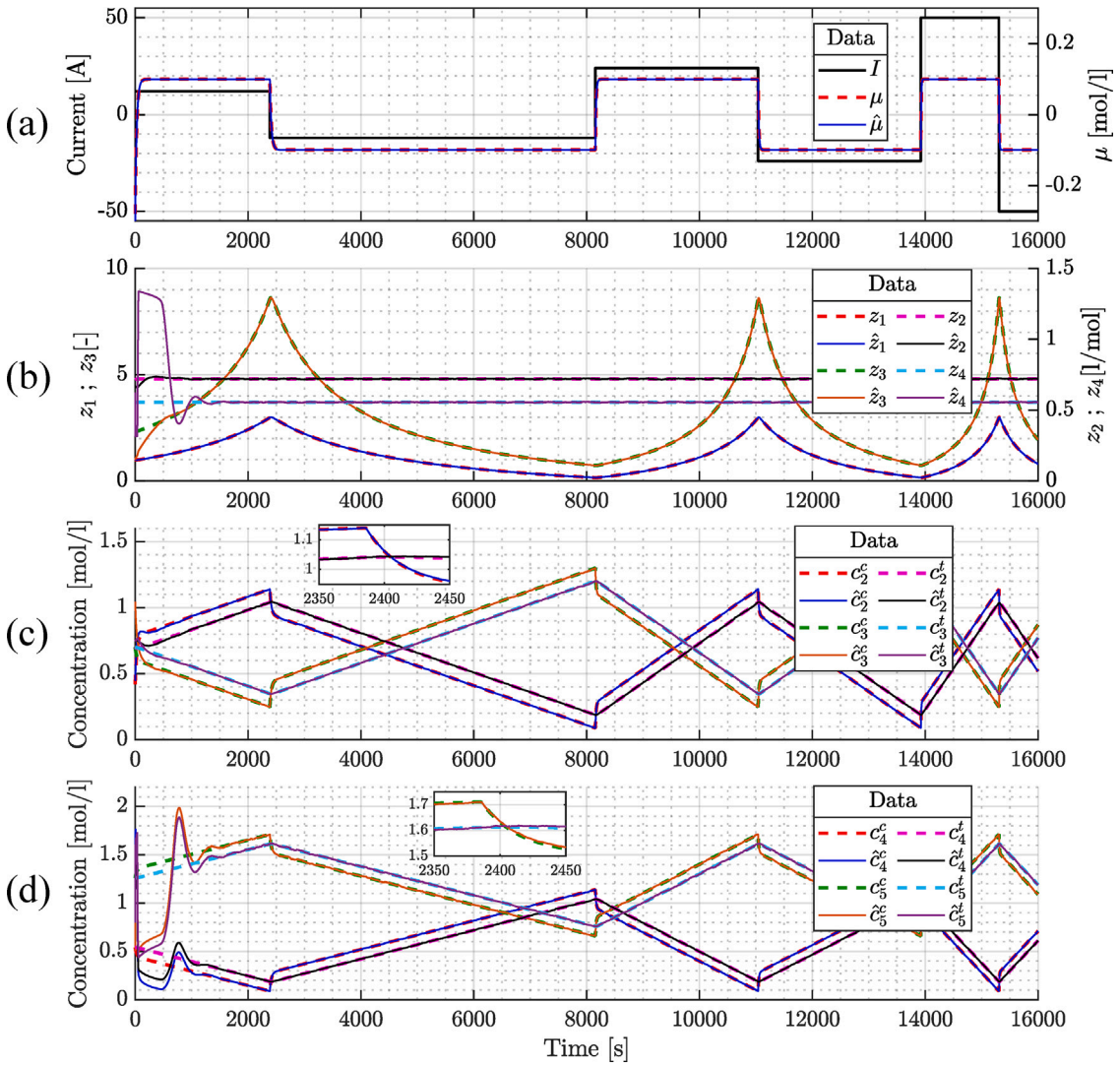

Fig. 3. Comparison between real and estimated states, in the different steps that compose the observer. (a) Tanks-Cells concentration difference (μ), together with the current profile. (b) States of the metric-based observer ($\mathbf{z}$). (c) Tank and cell concentrations in the negative side of the system (c_2 and c_3). (d) Tank and cell concentrations in the positive side of the system (c_4 and c_5).

a very short convergence time, the estimated $\hat{\mu}$ converges to the real μ, and accurately tracks it throughout the complete simulation period. During charge operation ($I > 0$), μ has a positive steady value, indicating that, as a consequence of the electrochemical reactions, the concentrations of V^{2+} and V^{5+} in the cells are higher than in the tanks, while the concentrations of V^{3+} and V^{4+} are lower. Consistently, the opposite behaviour is observed during the discharge operation ($I < 0$). Fig. 3b shows the outputs generated by the main observer (29), which employs the estimated $\hat{\mu}$ together with the current, voltages and flow rate measurements, to provide estimates of the transformed states, $\mathbf{z}$ (step 2 of Section 4.4). The estimated states take approximately 1200 s to converge to the real states, and accurately track them throughout the remainder of the test. This result is highly satisfactory, since no information regarding the initial imbalance of the system was available to the observer at the beginning of the simulation.

Finally, Figs. 3c and 3d show the reconstruction of the concentrations of the vanadium species present in the positive and negative side of the system, respectively. These are obtained by computing the inverse transformation from the $\hat{\mathbf{z}}$ states (steps 3 and 4 of Section 4.4). As expected, the convergence of $\hat{\mathbf{x}}$ is attained at the same time as $\hat{\mathbf{z}}$, given the direct relation between these two coordinates. After that transient, the estimated concentrations very accurately track the real ones, with a mean relative error below 1%. It should be highlighted that, even in the initial transient, the estimated concentrations remain within a realistic range. This is because of the inclusion of the flow redesign factor $\mathbf{M}$ in the observer, which prevents the states from reaching unrealistic values, such as negative concentrations or extremely high concentrations. This modification allows to preserve the numerical stability of the observer independently from the initial condition.

As outlined in Section 4, a notable advantage of the developed observer is that it does not require prior information regarding the system state. i.e., that the estimated initial conditions $\hat{\mathbf{x}}_0$ can be far from the real ones without compromising its stability and convergence. This property proves particularly significant for the studied system, where obtaining accurate initial conditions information is often impractical or impossible. The importance of this property is further analysed in Fig. 4. In that figure, the performance of the developed observer is compared with a classic EKF (Bernard et al., 2021). The structure of the EKF algorithm used in this demonstration is:

$$\dot{\hat{\mathbf{x}}} = \mathbf{f}(\hat{\mathbf{x}}, I, q) + \mathbf{P}\frac{\partial \mathbf{h}}{\partial \mathbf{x}}(\hat{\mathbf{x}})^{\top}\mathbf{R}^{-1}(y - \mathbf{h}(\hat{\mathbf{x}})) \tag{35a}$$

$$\dot{\mathbf{P}} = -\beta\mathbf{P} + \frac{\partial \mathbf{f}}{\partial \mathbf{x}}(\hat{\mathbf{x}}, I, q)\mathbf{P} + \mathbf{P}\frac{\partial \mathbf{f}}{\partial \mathbf{x}}(\hat{\mathbf{x}}, I, q)^{\top} - \mathbf{P}\frac{\partial \mathbf{h}}{\partial \mathbf{x}}(\hat{\mathbf{x}})^{\top}\mathbf{R}^{-1}\frac{\partial \mathbf{h}}{\partial \mathbf{x}}(\hat{\mathbf{x}})\mathbf{P}, \tag{35b}$$

with $\beta = 0.003$, $\mathbf{R^{-1}} = 0.5 \cdot \mathbf{I_2}$ and $\mathbf{P_0} = 1.2 \cdot \mathbf{I_8}$

Fig. 4a displays the estimated concentrations in the negative side of the system when the initial estimation states are placed close to the real

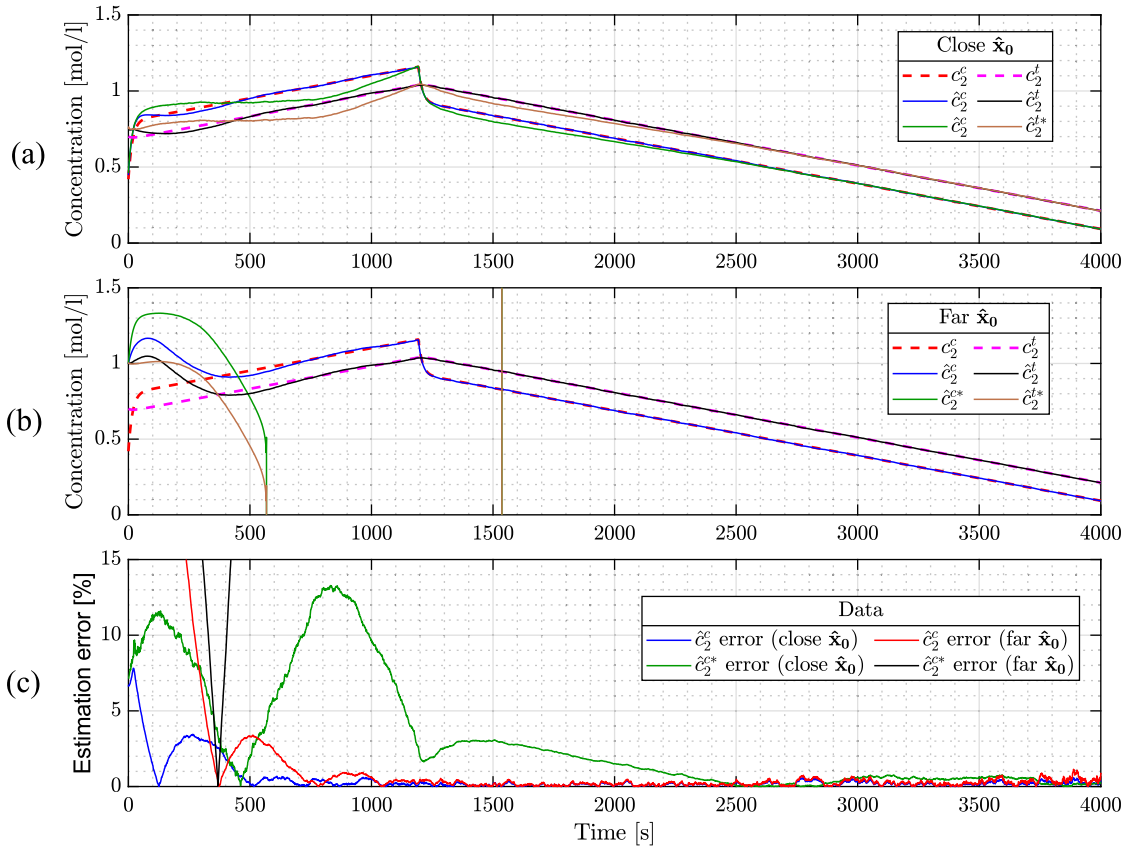

Fig. 4. Comparison between the performance of the observer designed in this paper and a classical EKF (estimates provided by the EKF are indicated with the superscript "$*$")(a) Close initial conditions (b) Far initial conditions (c) Relative estimation error of c_2^c, in cases (a) and (b).

states: $\hat{\mathbf{x}}_0 = [0.46\ 0.75\ 0.6\ 1.2\ 0.75\ 0.75\ 0.6\ 1.2]^\top$. It can be appreciated that both observers are able to converge to the real concentrations after a certain transient period, although this convergence is slower in the case of the estimates provided by the EKF (indicated in the figure with the superscript "$*$"). On the other hand, in Fig. 4b it is shown the estimation when the initial estimates are placed far from the real states: $\hat{\mathbf{x}}_0 = [1\ 1\ 1\ 1\ 1\ 1\ 1\ 1]^\top$, which corresponds to a situation in which no prior information is available. In the case of the observer developed in this paper, the only effect of this far initialisation is to extend the initial transient, without affecting its stability and performance. In contrast, the same initial conditions lead to a complete failure of the EKF algorithm, which is unable to converge to the real concentrations. Finally, the comparison between the relative estimation error for c_2^c in these two situations is displayed in Fig. 4c.

It should be remarked that there may exist a different set of parameters for the EKF that result in a better performance. However, there is not a systematic procedure to obtain those parameters and, furthermore, the stability issues when the initialisation is far from the real state cannot be eliminated through any parameter tuning.

5.2. Varying conditions test

The second set of simulations is designed to test the capacity of the observer to deal with more challenging conditions, which include intervals of zero current, a fluctuating flow rate, and a varying load profile. To this end, the simulation has been divided into three parts, to cover all these possible situations. To facilitate the comprehension of this section and avoid the need of excessively lengthy discussion, the analysis will be focused on the estimation of c_2^t and c_2^c.

The first part of the test covers the initial 2800 s of the simulation and consists of a charge/discharge operation with an intermittent current (see Fig. 5a). This is, in principle, a delicate condition from the theoretical point of view, given the non-observability of the system when the current approaches zero. However, as anticipated in Section 4.3, the algorithm is able to converge, since the error reduces when the current is different from zero, and the estimation error is constant while I is equal to 0. In Fig. 5b, it can be appreciated that the tanks and cells concentrations tend to equalise when the current is equal to 0, and separate again when the battery is being charged or discharged. In both situations, the concentrations are successfully estimated by the observer, with a relative error remaining below 1.9% after the initial transient (see Fig. 5c).

In the second part of the simulation, the battery is operated with a constant current and a fluctuating flow rate, which ranges from 12 ml/s to 36 ml/s (see Fig. 5a). In Fig. 5b it can be noted that, when the flow rate is high (e.g., at $t = 3000$ s), the reactant supply largely exceeds the consumption of the electrochemical reactions, hence there is little difference between tank and cell concentrations. On the contrary, when the flow rate is low (e.g., at $t = 3500$ s), the difference between tank and cell concentrations becomes much more important. In any case, the observer is able to successfully deal with this varying flow rate, and maintain the estimation error below 1% during this part of the simulation.

Finally, a continuously varying current profile is considered. This case has a particular practical significance, given that this type of variations can be found in a wide range of applications, such as in microgrids based on renewable energy sources. In spite of these demanding conditions, the performance of the observer is highly satisfactory, showing no loss of accuracy when compared to the constant current case.

5.3. Flow rate optimisation strategy

As previously discussed, estimating the vanadium species concentrations is not only essential to monitor the VFB status and planning

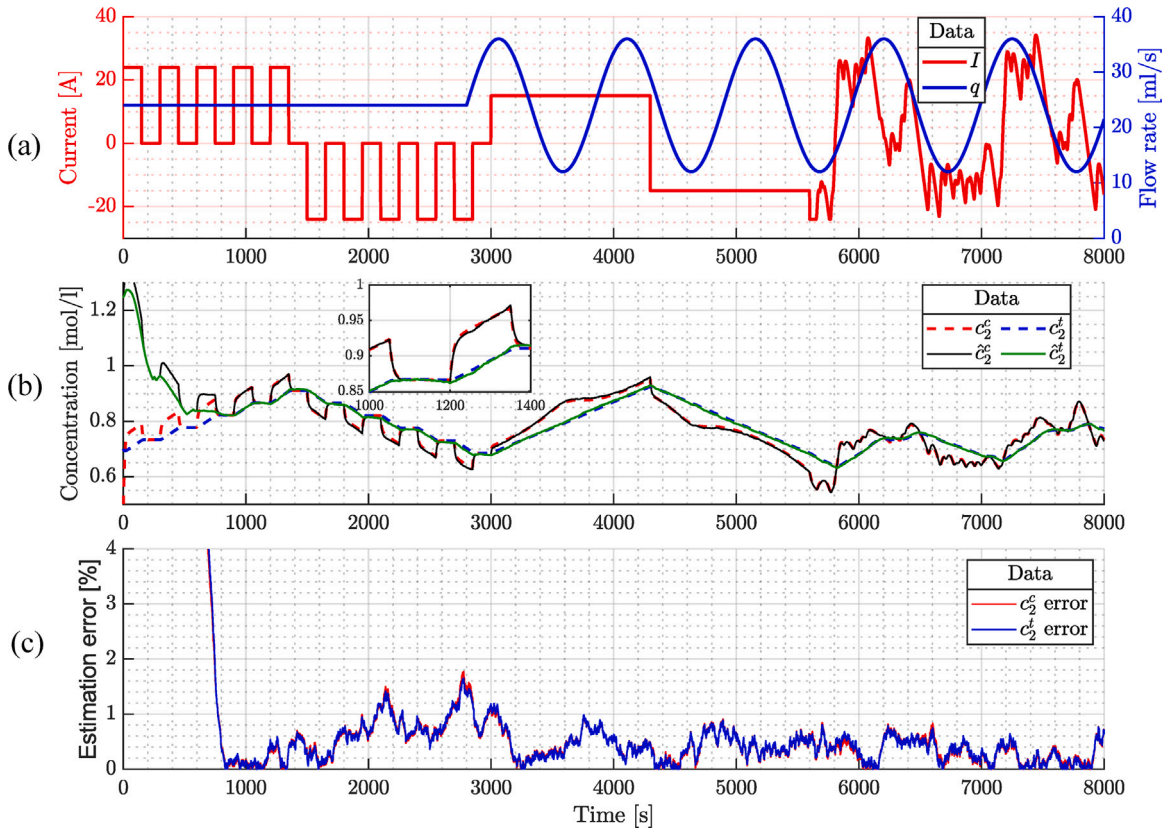

Fig. 5. Results under highly varying operating conditions. (a) Current and flow rate profiles. (b) Estimation of the evolution of c_2^c and c_2^t. (c) Relative estimation error.

its operation, but also to develop improved control and optimisation strategies to enhance the battery's performance. In this subsection, we illustrate the importance of this latter aspect by proposing a flow rate regulation strategy that considers the electrolyte imbalance.

In general, flow rate modulation strategies aim to minimise the total energy losses by adapting q to the power demand and the SoC (Guarnieri et al., 2020; König et al., 2016). In a balanced VFB, the SoC is defined as the fraction of vanadium "charged species"(V^{2+} and V^{5+}), with respect to the total concentration, as follows (Puleston et al., 2022):

$$\text{SoC} = \frac{v_t\, c_2^t + m\, v_c c_2^c}{v_t\, c_2^t + m v_c c_2^c + v_t\, c_3^t + m v_c c_3^c} = \frac{v_t\, c_5^t + m\, v_c c_5^c}{v_t\, c_4^t + m v_c c_4^c + v_t\, c_2^t + m v_c c_2^c} \tag{36}$$

However, when the VFB suffers from electrolyte imbalance, Eq. (36) is no longer valid, and it becomes necessary to define a individual SoC for each side of the system:

At the negative side:
$$\text{SoC}_\text{n} = \frac{v_t\, c_2^t + m\, v_c c_2^c}{v_t\, c_2^t + m\, v_c c_2^c + v_t\, c_3^t + m\, v_c c_3^c} \tag{37}$$

At the positive side:
$$\text{SoC}_\text{p} = \frac{v_t\, c_5^t + m\, v_c c_5^c}{v_t\, c_4^t + m\, v_c c_4^c + v_t\, c_2^t + m\, v_c c_2^c} \tag{38}$$

The theoretical minimum flow of electrolyte (q_{min}) is such that it provides the cells with a reactant supply that is exactly the same as the consumption of the electrochemical reactions:

$$q_{min} = \begin{cases} \dfrac{mI}{F(1-\text{SoC})c_{v_0}} & \text{for charging} \quad (39a) \\ \dfrac{m|I|}{F\ \text{SoC}\ c_{v_0}} & \text{for discharging} \quad (39b) \end{cases}$$

In practice, however, a higher supply is required to guarantee that enough reactant will reach the electrodes active sites, as well as to reduce concentration overpotentials and minimise the risk of side reactions such as hydrogen evolution. Therefore, a "flow factor" α_F that links the real flow rate (q) with q_{min} can be defined as follows: $\alpha_F = q/q_{min}$.

If the system is imbalanced, Eq. (39) is still valid, but there will be a different q_{min} for each electrolyte. Thus, based on the information provided by the observer, we propose to regulate independently both flow rates to adapt it to the existing electrolyte imbalance of the battery. It should be mentioned that in a real application this strategy will be combined with a safety layer that, taking into account the mechanical properties of the cell, will be responsible for preventing unacceptable pressure differences. For the purposes of this paper, it is assumed that the system is operating within the safe zone. Succinctly, the steps of the proposed strategy are:

1. To determine the system concentrations using the observer developed in Section 4.
2. To compute SoC_n and SoC_p using the estimated concentrations.
3. To determine the minimum flow rate for each electrolyte by applying (39). Note that, instead of c_{v_0}, the actual concentration of the imbalanced electrolyte must be used.
4. To independently set the flow rate for each electrolyte, applying the corresponding α_F. In this paper, a typical value of $\alpha_F = 5$ is considered to illustrate the proposal. The development of enhanced approaches for determining the optimal α_F is a topic of interest for future investigation.

Fig. 6 presents the results of applying the proposed flow rate regulation strategy. Starting from an imbalanced initial condition, the observer is able to provide reliable estimates of the individual state of charge of each electrolyte (see Fig. 6a). Fig. 6b shows the resulting flow rates, determined by applying a flow factor of 5 to the minimum flow rates calculated with the estimated SoC_n and SoC_p. Note that q_n and

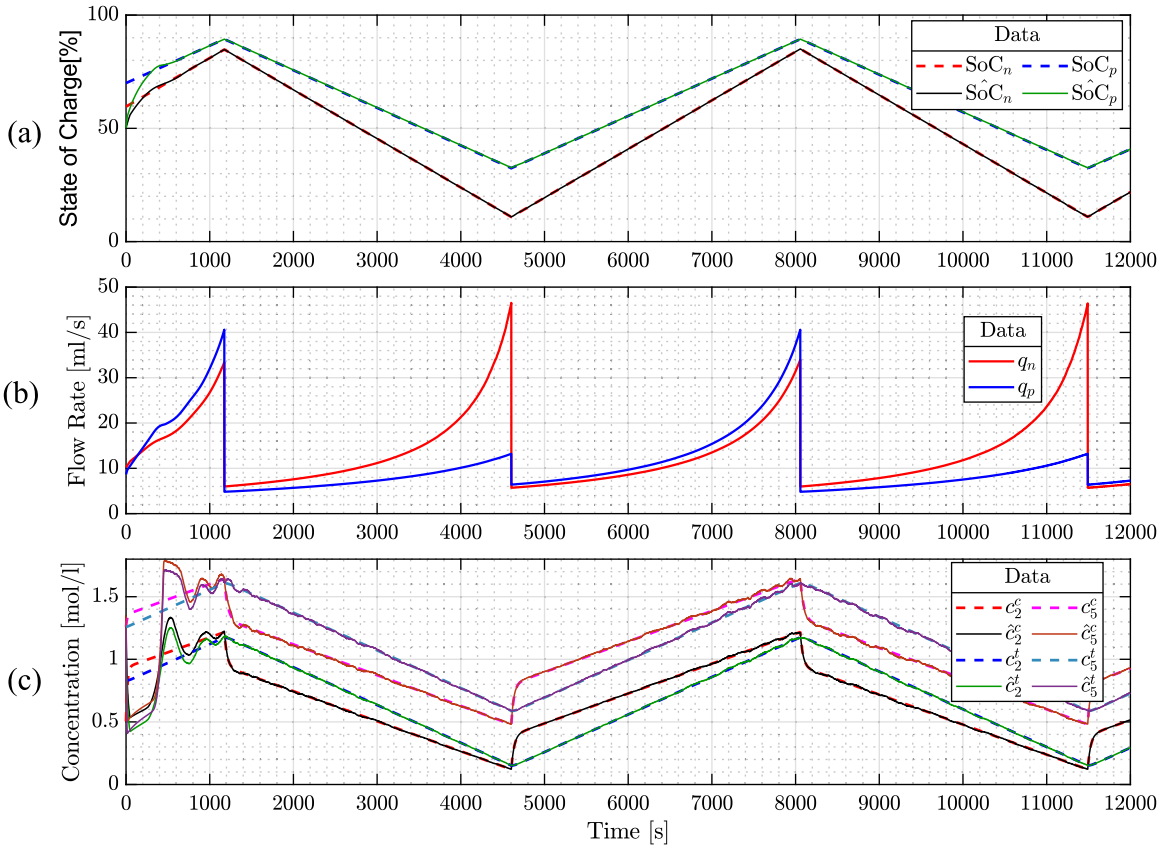

Fig. 6. Demonstration of the observer-based flow rate optimisation strategy. (a) Estimation of the individual State of Charge of the positive and negative electrolytes. (b) Flow rate profiles of the negative (q_n) and positive (q_p) electrolytes. (c) Comparison between actual and estimated V^{2+} and V^{5+} concentrations in tanks and cells.

q_p can be significantly different, which is due to the fact that, when imbalanced, the reactant concentration in one electrolyte is in excess with respect to the one in the other. This difference is more pronounced by the end of the charge/discharge operations, when a larger flow rate is needed to compensate the low reactant concentrations. By adapting q_n and q_p to the electrolyte imbalance, the flow rate in the side with a reactant excess can be set at a lower value without affecting the electrochemical performance of the battery, hence resulting in a reduction of the pumping power demand.

Finally, Fig. 6c displays the evolution of the real and estimated V^{2+} and V^{5+} concentrations, both in tanks and cells. It can be appreciated that when the flow rate is higher, i.e., by the end of the charge and discharge operations, the difference between tanks and cell concentration becomes lower. Consequently, this strategy based on varying flow rates allows to operate the battery within a wider SoC window, extending the actual capacity of the VFB. For instance, if a constant flow rate of 12 ml/s was utilised, c_2^c would have reached a concentration close to 0 at time 4000 s, thus impeding to continue with the discharge operation.

6. Conclusions

A novel nonlinear observer has been developed for the online estimation of the four active species concentrations present in vanadium flow batteries. The observer relies only on current, flow rates and half-cell cell voltage measurements. The proposal distinguishes itself from previous works in the field by effectively addressing two challenging and significant conditions simultaneously. On the one hand, it is able to properly deal with the electrolyte imbalance that typically affect VFB systems, without requiring previous information regarding the mass imbalance or the average oxidation state. On the other hand, it allows to differentiate between tanks and cells concentrations, which becomes particularly relevant when the flow rate cannot be considered "very high", such as when the flow rate is being controlled to optimise the battery performance.

Through comprehensive computer simulation, it has been demonstrated that the observer presents a remarkable robustness to model uncertainties and measurement noise. Specifically, once the initial transient has elapsed, it has been able to keep the estimation relative error below 1.9% even under highly varying operating conditions. Furthermore, it has been theoretically demonstrated and practically validated that, unlike observer based on model linearisation, the stability and convergence of the algorithm is not affected by its initial conditions, which constitutes a key advantage when no prior information regarding the system state is available. In addition, the algorithm allows the utilisation of physical constraints, to accelerate the convergence and keep the estimates within a realistic range, even during the transients. Lastly, the importance of knowing the individual vanadium species concentrations has been illustrated with the development of an strategy to independently regulate the flow rate in each side of the system based on the estimated state of charge of each electrolyte.

In conclusion, the above mentioned features, together with a simple parameter tuning and low-cost equipment requirements, results in a new estimation solution very auspicious for implementation in industrial applications. As future research, the authors are considering to combine the proposed observer with setups for online estimation of the side-reaction parameters and overpotential parameters. In addition, an estimation algorithm for tracking possible variations of the reference electrodes potentials is being undertaken, in order to circumvent their recalibration. Further development of interest in the field are, on the one hand, an in-depth study on the effects of possible non-uniform composition of the electrolyte's tanks. On the other, the development of enhanced control strategies that, based on the information provided by the observer, would allow not only to optimise the battery efficiency, but also to minimise its degradation.

CRediT authorship contribution statement

Thomas Puleston: Writing – original draft, Software, Methodology, Investigation, Formal analysis, Conceptualization. **Andreu Cecilia:** Writing – original draft, Methodology, Investigation, Formal analysis, Conceptualization. **Ramon Costa-Castelló:** Writing – review & editing, Validation, Supervision, Project administration, Funding acquisition. **Maria Serra:** Writing – review & editing, Validation, Supervision, Resources, Project administration, Funding acquisition.

Declaration of competing interest

The authors declare that they have no known competing financial interests or personal relationships that could have appeared to influence the work reported in this paper.

Data availability

Data will be made available on request.

Acknowledgements

The project that gave rise to these results received the support of a fellowship from "la Caixa" Foundation, Spain (ID 100010434). The fellowship code is LCF/BQ/DI21/11860023. This research was also supported by the Spanish Ministry of Science and Innovation, under the projects MAFALDA (PID2021-126001OB-C31) and MASHED (TED2021-129927B-I00). This work has been supported by the Spanish Ministry of Universities funded by the European Union - NextGenerationEU (2022UPC-MSC-93823).

Appendix A. μ Dynamics symmetry proof

The objective is to prove that $\mu_2(t)$ asymptotically converges to $-\mu_1(t)$ regardless of the initial conditions. Furthermore, if $\mu_2(0) = -\mu_1(0)$, then $\mu_2(t) = -\mu_1(t)$ for all $t \geq 0$.

Taking $\alpha_1 := q_n(\frac{1}{m v_c} + \frac{1}{v_t})$ and $\alpha_2 := \frac{I}{F v_c}$, the dynamics for μ estimates can be expressed as:

$$\begin{cases} \dot{\mu}_1 = -\alpha_1 \mu_1 + \alpha_2 & \text{(A.1a)} \\ \dot{\mu}_2 = -\alpha_1 \mu_2 - \alpha_2 & \text{(A.1b)} \end{cases}$$

Then, we have that:

$$\dot{\mu}_1 + \dot{\mu}_2 = -\alpha_1(\mu_1 + \mu_2). \tag{A.2}$$

Separating variables and integrating, we obtain:

$$\mu_1(t) + \mu_2(t) = (\mu_1(0) + \mu_2(0))e^{-\alpha_1 t}. \tag{A.3}$$

It is possible to see that, the exponential term of (A.3) will make $\mu_1(t)$ and $\mu_2(t)$ to asymptotically converge to each other, regardless of the initial conditions $\mu_1(0)$ and $\mu_2(0)$. Additionally, if $\mu_2(0) = -\mu_1(0)$, then the right-hand side of (A.3) will be equal to zero, which implies that $\mu_2(t) = -\mu_1(t)$ for all $t \geq 0$, so that the left hand side is also zero.

Appendix B. Nonlinear observer convergence proof

In this section, we prove the convergence of the observer (29). As a first remark of the proof, we will show that the observer is stable with a quadratic Lyapunov function for the case $\mathbf{M}(\hat{\mathbf{z}}) = 0$. The stability for the case of $\mathbf{M}(\hat{\mathbf{z}})$ being defined as in (31), follows from the fact that the observer is stable with a quadratic Lyapunov function with the constant metric $\mathbf{P}(\mathbf{u})$ defined in (32) and the theory presented in Astolfi et al. (2022).

As a second remark, we will assume $u_n \neq 0$. In Section 4.3, we already show that, in the case $u_n = 0$, the estimation error does not converge to zero, but remains constant. In this section, we focus in showing that the estimation error converges to zero if $u_n \neq 0$.

As a final remark, we will focus in only one side of the VFB. Since the model and the observer are symmetric, the proof for one side is equivalent to the proof of the other side.

We recall that the model of one side of the VFB is

$$\dot{z} = \begin{bmatrix} u_n z_2 (1 + z_1)^2 \\ 0 \end{bmatrix} = \begin{bmatrix} a(t) z_2 \\ 0 \end{bmatrix},$$

where $a(t) := u_n(t)(1 + z_1(t))^2$. Notice that here we take $u_n(t)$ and $z_1(t)$ as time-varying and measurable signals. Since we assumed that $u_n \neq 0$ and, from the physical constraints of the system, $z_1 \geq 0$, we have $a(t) \neq 0$ for all $t \geq 0$.

The proposed observer (with $\mathbf{M}(\hat{\mathbf{z}}) = 0$) for this side is

$$\dot{\hat{\mathbf{z}}} = \begin{bmatrix} a(t)\hat{z}_2 \\ 0 \end{bmatrix} + \begin{bmatrix} l\lambda_{1,n}[y_1 - \hat{z}_1] \\ l\lambda_{2,n}(u_n)[y_1 - \hat{z}_1] \end{bmatrix},$$

where l is a large enough positive constant ($l \geq 1$), $\lambda_{1,j} > 3|u_n(t)(1 + z_1(t))^2|$, with $j \in \{n, p\}$ and $\lambda_{2,j}(u_j) = \lambda_{1,j}\ \mathrm{sgn}(u_j)$.

Now, define the error variable $\tilde{\mathbf{z}} := \mathbf{z} - \hat{\mathbf{z}}$ and notice that the error dynamics are depicted by

$$\dot{\tilde{\mathbf{z}}} = \begin{bmatrix} -l\lambda_{1,n} & a(t) \\ -l\lambda_{2,n}(u_n) & 0 \end{bmatrix} \tilde{\mathbf{z}} := \mathbf{A}(t)\tilde{\mathbf{z}}. \tag{B.1}$$

We define the following symmetric positive definite matrix

$$\mathbf{P}(\mathbf{u}) := \begin{bmatrix} 8 & -\mathrm{sgn}(u_n) \\ -\mathrm{sgn}(u_n) & 1 \end{bmatrix},$$

where $\mathrm{sgn}(\cdot)$ is the sign function with $\mathrm{sgn}(0) = 0$. We highlight that $\mathbf{P}(\mathbf{u})$ is positive definite for any value of $\mathbf{u}$. Moreover, even if this matrix depends on $\mathbf{u}$, we have $\dot{\mathbf{P}} = 0$ since the sign function is a piecewise-constant function and we focus in the scenario $u_n \neq 0$.

Consider the Lyapunov function candidate

$$V = \tilde{\mathbf{z}}^\top \mathbf{P}(\mathbf{u})\tilde{\mathbf{z}}. \tag{B.2}$$

Then, the derivative of (B.2) along the error dynamics (B.1) satisfies

$$\dot{V} = \tilde{\mathbf{z}}^\top (\mathbf{A}(t)^\top \mathbf{P}(\mathbf{u}) + \mathbf{P}(\mathbf{u})\mathbf{A}(t))\tilde{\mathbf{z}}^\top < 0. \tag{B.3}$$

Therefore, following standard Lyapunov arguments, we can conclude that the error dynamics (B.1) are globally asymptotically stable, which proves the convergence of the observer. To see the inequality (B.3), notice the following:

$$\mathbf{A}(t)^\top \mathbf{P}(\mathbf{u}) + \mathbf{P}(\mathbf{u})\mathbf{A}(t) = \begin{bmatrix} 2(-8l\lambda_{1,n} + l\lambda_{2,n}(u_n)\mathrm{sgn}(u_n)) & \mathrm{sgn}(u_n)l\lambda_{1,n} - l\lambda_{2,n}(u_n) + 8a(t) \\ \mathrm{sgn}(u_n)l\lambda_{1,n} - l\lambda_{2,n}(u_n) + 8a(t) & -2\mathrm{sgn}(u_n)a(t) \end{bmatrix}$$

Notice that we have $\lambda_{2,j}(u_j) = \lambda_{1,j}\ \mathrm{sgn}(u_j)$ by definition. Moreover, since $z_1, z_2 \geq 0$, we have that $\mathrm{sgn}(u_n) = \mathrm{sgn}(a(t))$. Therefore, we get the following equality,

$$\mathbf{A}(t)^\top \mathbf{P}(\mathbf{u}) + \mathbf{P}(\mathbf{u})\mathbf{A}(t) = \begin{bmatrix} -14l\lambda_{1,n} & 8a(t) \\ 8a(t) & -2|a(t)| \end{bmatrix}. \tag{B.4}$$

The matrix in the right-hand side of (B.4) will be negative definite if its trace is negative and the determinant is positive. Since $\lambda_{1,n}, l > 0$ the trace is negative. On the other hand, the determinant is

$$28l\lambda_{1,n}|a(t)| - 64a(t)^2,$$

which will be positive if $l \geq 1$ and $\lambda_{1,j} > 3|a(t)| = 3|(u_n(t)(1 + z_1(t))^2)|$. Finally, the negativity of the determinant, shows that the inequality (B.4) is negative and, thus, (B.3) is satisfied, which ends the proof.

References

Akter, M.P., Li, Y., Bao, J., Skyllas-Kazacos, M., Rahman, M.F., 2019. Optimal charging of vanadium redox flow battery with time-varying input power. Batteries 5, http://dx.doi.org/10.3390/batteries5010020.

Astolfi, D., Bernard, P., Postoyan, R., Marconi, L., 2022. Constrained state estimation for nonlinear systems: A redesign approach based on convexity. IEEE Trans. Automat. Control 67, 824–839. http://dx.doi.org/10.1109/TAC.2021.3064537.

Bernard, P., Andrieu, V., Astolfi, D., 2022. Observer design for continuous-time dynamical systems. Annu. Rev. Control 53, 224–248. http://dx.doi.org/10.1016/j.arcontrol.2021.11.002.

Bernard, P., Mimmo, N., Marconi, L., 2021. On the semi-global stability of an EK-like filter. IEEE Control Syst. Lett. 5 (5), 1771–1776. http://dx.doi.org/10.1109/LCSYS.2020.3044030.

Bogdanov, S., Pugach, M., Parsegov, S., Vlasov, V., Ibanez, F.M., Stevenson, K.J., Vorobev, P., 2023. Dynamic modeling of vanadium redox flow batteries: Practical approaches, their applications and limitations. J. Energy Storage 57, 106191. http://dx.doi.org/10.1016/j.est.2022.106191.

Cecchetti, M., Toja, F., Casalegno, A., Zago, M., 2023. A comprehensive experimental and modelling approach for the evaluation of cross-over fluxes in vanadium redox flow battery. J. Energy Storage 68, http://dx.doi.org/10.1016/j.est.2023.107846.

Choi, J., Park, W.-K., Lee, I.-W., 2016. Application of vanadium redox flow battery to grid connected microgrid energy management. In: 2016 IEEE International Conference on Renewable Energy Research and Applications. ICRERA, pp. 903–906. http://dx.doi.org/10.1109/ICRERA.2016.7884466.

Clemente, A., Cecilia, A., Costa-Castelló, R., 2023. Online state of charge estimation for a vanadium redox flow battery with unequal flow rates. J. Energy Storage 60, http://dx.doi.org/10.1016/j.est.2022.106503.

Clemente, A., Costa-Castelló, R., 2020. Redox flow batteries: A literature review oriented to automatic control. Energies 13 (17), http://dx.doi.org/10.3390/en13174514.

Clemente, A., Montiel, M., Barreras, F., Lozano, A., Costa-Castelló, R., 2021. Vanadium redox flow battery state of charge estimation using a concentration model and a sliding mode observer. IEEE Access 9, 72368–72376. http://dx.doi.org/10.1109/ACCESS.2021.3079382.

Cremoncini, D., Frate, G.F., Bischi, A., Ferrari, L., 2023. Mixed integer linear program model for optimized scheduling of a vanadium redox flow battery with variable efficiencies, capacity fade, and electrolyte maintenance. J. Energy Storage 59, 106500. http://dx.doi.org/10.1016/j.est.2022.106500.

Fornaro, P., Puleston, T., Puleston, P., Battaiotto, P., Costa-Castelló, R., Serra, M., 2023. Electric vehicle charging station based on wind energy: Evaluation of the power profile for vanadium redox flow batteries estimation. IEEE Latin Am. Trans. 21 (9), 1056–1062. http://dx.doi.org/10.1109/TLA.2023.10251813.

Fornaro, P., Puleston, T., Puleston, P., Serra-Prat, M., Costa-Castelló, R., Battaiotto, P., 2022. Redox flow battery time-varying parameter estimation based on high-order sliding mode differentiators. Int. J. Energy Res. 46 (12), 16576–16592. http://dx.doi.org/10.1002/er.8319.

Geiser, J., Natter, H., Hempelmann, R., Morgenstern, B., Hegetschweiler, K., 2019. Photometrical determination of the state-of-charge in vanadium redox flow batteries part I: In combination with potentiometric titration. Zeitschrift für Physikalische Chemie 233 (12), 1683–1694. http://dx.doi.org/10.1515/zpch-2019-1379.

Guarnieri, M., Trovò, A., D'Anzi, A., Alotto, P., 2018. Developing vanadium redox flow technology on a 9-kW 26-kWh industrial scale test facility: Design review and early experiments. Appl. Energy 230, 1425–1434. http://dx.doi.org/10.1016/j.apenergy.2018.09.021.

Guarnieri, M., Trovò, A., Picano, F., 2020. Enhancing the efficiency of kW-class vanadium redox flow batteries by flow factor modulation: An experimental method. Appl. Energy 262, http://dx.doi.org/10.1016/j.apenergy.2020.114532.

Haisch, T., Ji, H., Weidlich, C., 2020. Monitoring the state of charge of all-vanadium redox flow batteries to identify crossover of electrolyte. Electrochim. Acta 336, http://dx.doi.org/10.1016/j.electacta.2019.135573.

He, Q.Z., Stinis, P., Tartakovsky, A.M., 2022. Physics-constrained deep neural network method for estimating parameters in a redox flow battery. J. Power Sources 528, http://dx.doi.org/10.1016/j.jpowsour.2022.231147.

Hermann, R., Krener, A., 1977. Nonlinear controllability and observability. IEEE Trans. Automat. Control 22 (5), 728–740. http://dx.doi.org/10.1109/TAC.1977.1101601.

Huang, Z., Mu, A., 2021. Research and analysis of performance improvement of vanadium redox flow battery in microgrid: A technology review. Int. J. Energy Res. 45, 14170–14193. http://dx.doi.org/10.1002/er.6716.

Jienkulsawad, P., Jirabovornwisut, T., Chen, Y.S., Arpornwichanop, A., 2020. Improving the performance of an all-vanadium redox flow battery under imbalance conditions: Online dynamic optimization approach. ACS Sustain. Chem. Eng. 8, 13610–13622. http://dx.doi.org/10.1021/acssuschemeng.0c02973.

Jirabovornwisut, T., Arpornwichanop, A., 2019. A review on the electrolyte imbalance in vanadium redox flow batteries. Int. J. Hydrogen Energy 44, 24485–24509. http://dx.doi.org/10.1016/j.ijhydene.2019.07.106.

Jirabovornwisut, T., Kheawhom, S., Chen, Y.S., Arpornwichanop, A., 2020. Optimal operational strategy for a vanadium redox flow battery. Comput. Chem. Eng. 136, http://dx.doi.org/10.1016/j.compchemeng.2020.106805.

Kebede, A.A., Kalogiannis, T., Mierlo, J.V., Berecibar, M., 2022. A comprehensive review of stationary energy storage devices for large scale renewable energy sources grid integration. Renew. Sustain. Energy Rev. 159, http://dx.doi.org/10.1016/j.rser.2022.112213.

Khaki, B., Das, P., 2021. An equivalent circuit model for vanadium redox batteries via hybrid extended Kalman filter and particle filter methods. J. Energy Storage 39, http://dx.doi.org/10.1016/j.est.2021.102587.

König, S., Suriyah, M.R., Leibfried, T., 2016. Innovative model-based flow rate optimization for vanadium redox flow batteries. J. Power Sources 333, 134–144. http://dx.doi.org/10.1016/j.jpowsour.2016.09.147.

Li, Y., Sun, L., Cao, L., Bao, J., Skyllas-Kazacos, M., 2021. Dynamic model based membrane permeability estimation for online SOC imbalances monitoring of vanadium redox flow batteries. J. Energy Storage 39, http://dx.doi.org/10.1016/j.est.2021.102688.

Loktionov, P., Konev, D., Pichugov, R., Petrov, M., Antipov, A., 2023. Calibration-free coulometric sensors for operando electrolytes imbalance monitoring of vanadium redox flow battery. J. Power Sources 553, http://dx.doi.org/10.1016/j.jpowsour.2022.232242.

Loktionov, P., Pichugov, R., Konev, D., Petrov, M., Pustovalova, A., Antipov, A., 2022. Operando UV/Vis spectra deconvolution for comprehensive electrolytes analysis of vanadium redox flow battery. J. Electroanal. Soc. 925, 116912. http://dx.doi.org/10.1016/j.jelechem.2022.116912.

Neyhouse, B.J., Tenny, K.M., Chiang, Y.-M., Brushett, F.R., 2021. Microelectrode-based sensor for measuring operando active species concentrations in redox flow cells. ACS Appl. Energy Mater. 4 (12), 13830–13840. http://dx.doi.org/10.1021/acsaem.1c02580.

Nolte, O., Volodin, I.A., Stolze, C., Hager, M.D., Schubert, U.S., 2021. Trust is good, control is better: A review on monitoring and characterization techniques for flow battery electrolytes. Mater. Horiz. 8, 1866–1925. http://dx.doi.org/10.1039/d0mh01632b.

Nourani, M., Dennison, C.R., Jin, X., Liu, F., Agar, E., 2019. Elucidating effects of faradaic imbalance on vanadium redox flow battery performance: Experimental characterization. J. Electrochem. Soc. 166, A3844–A3851. http://dx.doi.org/10.1149/2.0851915jes.

Pichugov, R., Loktionov, P., Pustovalova, A., Glazkov, A., Grishko, A., Konev, D., Petrov, M., Usenko, A., Antipov, A., 2023. Restoring capacity and efficiency of vanadium redox flow battery via controlled adjustment of electrolyte composition by electrolysis cell. J. Power Sources 569, http://dx.doi.org/10.1016/j.jpowsour.2023.233013.

Poli, N., Schäffer, M., Trovò, A., Noack, J., Guarnieri, M., Fischer, P., 2021. Novel electrolyte rebalancing method for vanadium redox flow batteries. Chem. Eng. J. 405, http://dx.doi.org/10.1016/j.cej.2020.126583.

Puleston, T., Cecilia, A., Costa-Castelló, R., Serra, M., 2023. Vanadium redox flow batteries real-time state of charge and state of health estimation under electrolyte imbalance condition. J. Energy Storage 68, http://dx.doi.org/10.1016/j.est.2023.107666.

Puleston, T., Clemente, A., Costa-Castelló, R., Serra, M., 2022. Modelling and estimation of vanadium redox flow batteries: A review. Batteries 8, http://dx.doi.org/10.3390/batteries8090121.

Puleston, T., Serra, M., Costa-Castelló, R., 2024. Vanadium redox flow battery capacity loss mitigation strategy based on a comprehensive analysis of electrolyte imbalance effects. Appl. Energy 355, 122271. http://dx.doi.org/10.1016/j.apenergy.2023.122271.

Ressel, S., Bill, F., Holtz, L., Janshen, N., Chica, A., Flower, T., Weidlich, C., Struckmann, T., 2018. State of charge monitoring of vanadium redox flow batteries using half cell potentials and electrolyte density. J. Power Sources 378, 776–783. http://dx.doi.org/10.1016/j.jpowsour.2018.01.006.

Rybalchenko, M., Quill, N., Buckley, D.N., Lynch, R.P., 2022. (Invited) state of charge monitoring of vanadium flow batteries using spectroscopic and electrochemical methods. ECS Trans. 109 (3), 131. http://dx.doi.org/10.1149/10903.0131ecst.

Schubert, C., Hassen, W.F., Poisl, B., Seitz, S., Schubert, J., Usabiaga, E.O., Gaudo, P.M., Pettinger, K.H., 2023. Hybrid energy storage systems based on redox-flow batteries: Recent developments, challenges, and future perspectives. Batteries 9, http://dx.doi.org/10.3390/batteries9040211.

Tang, A., Bao, J., Skyllas-Kazacos, M., 2011. Dynamic modelling of the effects of ion diffusion and side reactions on the capacity loss for vanadium redox flow battery. J. Power Sources 196, 10737–10747. http://dx.doi.org/10.1016/j.jpowsour.2011.09.003.

Tempelman, C.H., Jacobs, J.F., Balzer, R.M., Degirmenci, V., 2020. Membranes for all vanadium redox flow batteries. J. Energy Storage 32, http://dx.doi.org/10.1016/j.est.2020.101754.

Wang, H., Pourmousavi, S.A., Soong, W.L., Zhang, X., Ertugrul, N., 2023. Battery and energy management system for vanadium redox flow battery: A critical review and recommendations. J. Energy Storage 58, http://dx.doi.org/10.1016/j.est.2022.106384.

Wei, Z., Tseng, K.J., Wai, N., Lim, T.M., Skyllas-Kazacos, M., 2016. Adaptive estimation of state of charge and capacity with online identified battery model for vanadium redox flow battery. J. Power Sources 332, 389–398. http://dx.doi.org/10.1016/j.jpowsour.2016.09.123.

Wei, Z., Xiong, R., Lim, T.M., Meng, S., Skyllas-Kazacos, M., 2018. Online monitoring of state of charge and capacity loss for vanadium redox flow battery based on autoregressive exogenous modeling. J. Power Sources 402, 252–262. http://dx.doi.org/10.1016/j.jpowsour.2018.09.028.

Xiong, B., Yang, Y., Tang, J., Li, Y., Wei, Z., Su, Y., Zhang, Q., 2019. An enhanced equivalent circuit model of vanadium redox flow battery energy storage systems considering thermal effects. IEEE Access 7, 162297–162308. http://dx.doi.org/10.1109/ACCESS.2019.2952212.

Xiong, B., Zhao, J., Su, Y., Wei, Z., Skyllas-Kazacos, M., 2017. State of charge estimation of vanadium redox flow battery based on sliding mode observer and dynamic model including capacity fading factor. IEEE Trans. Sustain. Energy 8, 1658–1667. http://dx.doi.org/10.1109/TSTE.2017.2699288.

Yan, L., Zang, X., Nie, Z., Zhong, L., Deng, Z.D., Wang, W., 2023. Online and noninvasive monitoring of battery health at negative-half cell in all-vanadium redox flow batteries using ultrasound. J. Power Sources 580, 233417. http://dx.doi.org/10.1016/j.jpowsour.2023.233417.

Yu, V., Headley, A., Chen, D., 2014. A constrained extended kalman filter for state-of-charge estimation of a vanadium redox flow battery with crossover effects. J. Dyn. Syst. Meas. Control Trans. ASME 136, http://dx.doi.org/10.1115/1.4026654.

Zang, X., Yan, L., Yang, Y., Pan, H., Nie, Z., Jung, K.W., Deng, Z.D., Wang, W., 2019. Monitoring the state-of-charge of a vanadium redox flow battery with the acoustic attenuation coefficient: An in operando noninvasive method. Small Methods 3 (12), 1900494. http://dx.doi.org/10.1002/smtd.201900494.

Zhang, Z., Ding, T., Zhou, Q., Sun, Y., Qu, M., Zeng, Z., Ju, Y., Li, L., Wang, K., Chi, F., 2021. A review of technologies and applications on versatile energy storage systems. Renew. Sustain. Energy Rev. 148, http://dx.doi.org/10.1016/j.rser.2021.111263.

Zhang, Y., Zhao, J., Wang, P., Skyllas-Kazacos, M., Xiong, B., Badrinarayanan, R., 2015. A comprehensive equivalent circuit model of all-vanadium redox flow battery for power system analysis. J. Power Sources 290, 14–24. http://dx.doi.org/10.1016/j.jpowsour.2015.04.169.

Zhao, X., Kim, K., Jung, S., 2022. State-of-charge estimation using data fusion for vanadium redox flow battery. J. Energy Storage 52, http://dx.doi.org/10.1016/j.est.2022.104852.

Zub, K., Stolze, C., Rohland, P., Stumpf, S., Hoeppener, S., Hager, M.D., Schubert, U.S., 2022. Inkjet-printed microband electrodes for a cost-efficient state-of-charge monitoring in redox flow batteries. Sensors Actuators B 369, http://dx.doi.org/10.1016/j.snb.2022.132291.